

1 **Metalloproteinase-dependent and TMPRSS2-independent cell surface entry**  
2 **pathway of SARS-CoV-2 requires the furin-cleavage site and the S2 domain of spike**  
3 **protein**

4

5

6 **Mizuki Yamamoto<sup>1</sup>, Jin Gohda<sup>1</sup>, Ayako Kobayashi<sup>1</sup>, Keiko Tomita<sup>1</sup>, Youko**  
7 **Hirayama<sup>1</sup>, Naohiko Koshikawa<sup>2</sup>, Motoharu Seiki<sup>3</sup>, Kentaro Semba<sup>4</sup>, Tetsu**  
8 **Akiyama<sup>5</sup>, Yasushi Kawaguchi<sup>1,6</sup> and Jun-ichiro Inoue<sup>7\*</sup>**

9 <sup>1</sup>Research Center for Asian Infectious Diseases, The Institute of Medical Science, The  
10 University of Tokyo, Tokyo 108-8639, Japan

11 <sup>2</sup>Department of Life Science and Technology, Tokyo Institute of Technology, Yokohama  
12 226-8501 Japan

13 <sup>3</sup>Division of Cancer Cell Research, The Institute of Medical Science, The University of  
14 Tokyo, Tokyo 108-8639, Japan

15 <sup>4</sup>Department of Life Science and Medical Bio-Science, Waseda University, Shinjuku-ku,  
16 Tokyo, 162-8480, Japan

17 <sup>5</sup>Laboratory of Molecular and Genetic Information, Institute for Quantitative Biosciences,  
18 The University of Tokyo, Tokyo 113-0032, Japan

19 <sup>6</sup>Division of Molecular Virology, Department of Microbiology and Immunology, The  
20 Institute of Medical Science, The University of Tokyo, Tokyo 108-8639, Japan

21 <sup>7</sup>Research Platform Office, The Institute of Medical Science, The University of Tokyo,  
22 Tokyo 108-8639, Japan

23

24 \* Corresponding author:

25 E-mail: [jun-i@ims.u-tokyo.ac.jp](mailto:jun-i@ims.u-tokyo.ac.jp) (JI)

26

27 **Abstract**

28 The ongoing global vaccination program to prevent SARS-CoV-2 infection, the causative  
29 agent of COVID-19, has had significant success. However, recently virus variants have  
30 emerged that can evade the immunity in a host achieved through vaccination.  
31 Consequently, new therapeutic agents that can efficiently prevent infection from these  
32 new variants, and hence COVID-19 spread are urgently required. To achieve this,  
33 extensive characterization of virus-host cell interactions to identify effective therapeutic  
34 targets is warranted. Here, we report a cell surface entry pathway of SARS-CoV-2 that  
35 exists in a cell type-dependent manner is TMPRSS2-independent but sensitive to various  
36 broad-spectrum metalloproteinase inhibitors such as marimastat and prinomastat.  
37 Experiments with selective metalloproteinase inhibitors and gene-specific siRNAs  
38 revealed that a disintegrin and metalloproteinase 10 (ADAM10) is partially involved in  
39 the metalloproteinase pathway. Consistent with our finding that the pathway is unique to  
40 SARS-CoV-2 among highly pathogenic human coronaviruses, both the furin cleavage  
41 motif in the S1/S2 boundary and the S2 domain of SARS-CoV-2 spike protein are  
42 essential for metalloproteinase-dependent entry. In contrast, the two elements of SARS-  
43 CoV-2 independently contributed to TMPRSS2-dependent S2 priming. The  
44 metalloproteinase pathway is involved in SARS-CoV-2-induced syncytia formation and

45 cytopathicity, leading us to theorize that it is also involved in the rapid spread of SARS-  
46 CoV-2 and the pathogenesis of COVID-19. Thus, targeting the metalloproteinase  
47 pathway in addition to the TMPRSS2 and endosome pathways could be an effective  
48 strategy by which to cure COVID-19 in the future.

49

## 50 **Author Summary**

51 To develop effective therapeutics against COVID-19, it is necessary to elucidate in detail  
52 the infection mechanism of the causative agent, SARS-CoV-2, including recently  
53 emerging variants. SARS-CoV-2 binds to the cell surface receptor ACE2 via the Spike  
54 protein, and then the Spike protein is cleaved by host proteases to enable entry. Selection  
55 of target cells by expression of these tissue-specific proteases contributes to pathogenesis.  
56 Here, we found that the metalloproteinase-mediated pathway is important for SARS-  
57 CoV-2 infection, variants included. This pathway requires both the prior cleavage of  
58 Spike into two domains and a specific sequence in the second domain S2, conditions met  
59 by SARS-CoV-2 but lacking in the related human coronavirus SARS-CoV. The  
60 contribution of several proteases, including metalloproteinases, to SARS-CoV-2  
61 infection was cell type dependent, especially in cells derived from kidney, ovary, and  
62 endometrium, in which SARS-CoV-2 infection was metalloproteinase-dependent. In

63 these cells, inhibition of metalloproteinases by treatment with marimastat or prinomastat,  
64 whose safety was previously confirmed in clinical trials, was important in preventing cell  
65 death. Our study provides new insights into the complex pathogenesis unique to COVID-  
66 19 and relevant to the development of effective therapies.

## 67 **Introduction**

68 Severe acute respiratory syndrome coronavirus 2 (SARS-CoV-2), the causative agent of  
69 coronavirus disease 2019 (COVID-19), was first recognized in late 2019 and led to the  
70 development of a global pandemic in 2020[1]. Two other human coronaviruses, SARS-  
71 CoV[2, 3] and Middle East respiratory syndrome coronavirus (MERS-CoV)[4], are also  
72 capable of inducing lethal pneumonia and systemic symptoms. However, SARS-COV-2  
73 has been found to also exhibit enhanced pathogenicity and transmissibility[5, 6].  
74 Effective vaccines have been developed, and ongoing global vaccination programs have  
75 significantly curbed the spread of infection[7, 8]. However, current vaccinations may  
76 provide imperfect protection as new variants of the virus that can spread more easily and  
77 evade the host immunity achieved through vaccination have been reported[7, 9-11].  
78 Furthermore, although several drugs that may provide effective treatments for COVID-  
79 19 are currently under clinical trial and awaiting approval[12, 13], it is currently unclear  
80 if daily life around the world will ever return to that of pre-COVID-19 times.  
81 Consequently, further extensive characterization of the virus and its interactions with host  
82 cells are required to develop vaccines and therapeutic agents that efficiently prevent  
83 infection from the new emerging highly infective variants so as to limit further worsening  
84 of COVID-19.

85           The initiation of SARS-CoV-2 entry requires two steps after its spike (S) protein  
86 is cleaved into S1 and S2 by furin-like proteases expressed in virus-producing cells prior  
87 to viral release[14-16]. First, the S protein binds to its receptor angiotensin converting  
88 enzyme 2 (ACE2) in the plasma membrane through its receptor-binding domain  
89 (RBD)[17, 18]. Second, the S2 protein is cleaved to generate S2' by either cell surface  
90 transmembrane serine protease 2 (TMPRSS2)[19] or endosomal protease cathepsin-  
91 B/L[19, 20]. This cleavage is called priming, and exposes the fusion peptide within S2',  
92 allowing it to stick into the plasma or endosomal membrane, resulting in fusion between  
93 the viral envelope and the cellular membrane (envelope fusion). This fusion allows viral  
94 RNA to enter the cytoplasm where it replicates. Whether SARS-CoV-2 viruses use the  
95 plasma membrane, the endosome pathway, or both is dependent on the cell type[19, 21,  
96 22]. Furin-mediated cleavage at the S1/S2 boundary leads to efficient viral entry into  
97 airway cells[15, 16], where the TMPRSS2-dependent surface entry route dominates  
98 endosomal entry[19, 23].

99           In this study, we screened for inhibitors of SARS-CoV-2 infection and identified  
100 a cell surface entry pathway of SARS-CoV-2 that is TMPRSS2-independent but  
101 sensitive to various metalloproteinase inhibitors. Interestingly, the metalloproteinase-  
102 dependent pathway requires both the furin cleavage motif in the S1/S2 boundary and the

103 S2 domain of SARS-CoV-2, which is unique to SARS-CoV-2. These results suggest that  
104 co-operation between furin and some metalloproteinases could be crucial for SARS-CoV-  
105 2 spread and disease development *in vivo*. Consequently, targeting the metalloproteinase-  
106 pathway in addition to the TMPRSS2 and cathepsin-B/L pathways could be an effective  
107 strategy to cure COVID-19.

108

## 109 **Results**

### 110 **TMPRSS2-independent membrane fusion induced by the S protein of SARS-CoV-2** 111 **is blocked by metalloproteinase inhibitors**

112 In this investigation, the screening system used to detect effective inhibitors of  
113 coronavirus infection included a quantitative cell fusion assay between effector cells  
114 expressing S protein and target cells expressing either ACE2 (for SARS-CoV and SARS-  
115 CoV-2)[24] or CD26 (for MERS-CoV)[25], with or without TMPRSS2 (S1a,b Fig).  
116 Quantitation was accomplished using the dual split chimeric reporter proteins (DSP)1-7  
117 and DSP8-11, which contain both *Renilla* luciferase (RL) and green fluorescent protein  
118 (GFP) variants[26]. The DSP assay quantifies the degree of membrane fusion between  
119 the effector cells expressing DSP1-7 and the target cells expressing DSP8-11 based on  
120 the RL activity (S1c Fig). During analysis with the DSP cell fusion assay, a significant

121 amount of ACE2-dependent but TMPRSS2-independent cell-cell fusion was induced by  
122 the S protein of SARS-CoV-2, but not by that of SARS- or MERS-CoV (Fig 1a,b).  
123 Consistent with this finding, the cell fusion with TMPRSS2 in the target cells induced by  
124 the S protein of SARS-CoV and MERS-CoV was completely blocked when TMPRSS2  
125 was inhibited with 1  $\mu$ M nafamostat, while approximately 20% of the fusion by the  
126 SARS-CoV-2 S protein remained, even in the presence of 10  $\mu$ M nafamostat (Fig 1c).  
127 This amount of residual fusion was almost equal to that induced by the SARS-CoV-2 S  
128 protein in the absence of TMPRSS2 (Fig 1d).

129 To explore the mechanism of TMPRSS2-independent membrane fusion, we  
130 screened the Validated Compound Library (1,630 clinically approved compounds and  
131 1,885 pharmacologically active compounds) obtained from the Drug Discovery Initiative  
132 (The University of Tokyo). We aimed to identify compounds that preferentially inhibited  
133 SARS-CoV-2 S protein-induced TMPRSS2-independent fusion and not TMPRSS2-  
134 dependent fusion. We compared the relative fusion values of the target cells expressing  
135 both TMPRSS2 and ACE2 (X-axis of Fig 2a) with those of the target cells expressing  
136 ACE2 alone (Y-axis of Fig 2a), and chose for further validation compounds that limited  
137 the fusion without TMPRSS2 by less than 60% and allowed the fusion with TMPRSS2  
138 by more than 70% (Fig 2a). The compounds selected included two metalloproteinase



139 inhibitors (ilomastat, CTS-1027), three tyrosine kinase inhibitors (sunitinib, PD-166285,  
140 PD-173952), two checkpoint kinase inhibitors (PF-477736, AZD-7762), a protein kinase  
141 C inhibitor (midostaurin), and a hormonal contraceptive (algestone). Ilomastat and CTS-  
142 1027 preferentially inhibited the TMPRSS2-independent fusion in a dose-dependent  
143 manner without affecting TMPRSS2-dependent fusion (Fig 2b). Furthermore, the  
144 luciferase activities of the preformed DSP1-7/DSP8-11 complex were not affected,  
145 confirming the specificity of the DSP assay (S2a,b Fig). However, other compounds  
146 inhibited both the TMPRSS2-dependent and -independent fusions to similar degrees (S3  
147 Fig). These data suggest that the metalloproteinase-dependent cell surface entry pathway  
148 (the metalloproteinase pathway) may be unique to SARS-CoV-2 among human  
149 pathogenic coronaviruses with high mortality rates. Considering that metalloproteinase  
150 inhibitors could thus possibly be used as prophylactic or therapeutic agents for COVID-  
151 19, we further demonstrated that marimastat[27] and prinomastat[28] (whose safety was  
152 previously confirmed in clinical trials to investigate their use as anticancer agents, such  
153 as CTS-1027[29]) can preferentially block the TMPRSS2-independent fusion induced by  
154 the SARS-CoV-2 S protein (Fig 2b and S2b Fig).

155

156 **The metalloproteinase pathway is SARS-CoV-2 specific and cell type-dependent**

157 We investigated whether the metalloproteinase pathway exists in SARS-CoV-2 S-bearing  
158 vesicular stomatitis virus (VSV) pseudovirus. The pseudovirus entry into the A704 cells  
159 (human kidney) was entirely blocked by 1  $\mu$ M marimastat (Fig 3a). This indicates that  
160 the metalloproteinase pathway is involved in the entry of the virus, and that 1  $\mu$ M  
161 marimastat could be used to determine if the pathway exists in other cells. Similarly, all  
162 entry pathways in OVISE cells (human ovary) were blocked by 25  $\mu$ M E-64d (Fig 3a),  
163 indicating that it could be used to investigate the existence of cathepsin-B/L-dependent  
164 endosome pathways in other cells. Furthermore, the entry pathways in Calu-3 cells  
165 (human lung) were entirely blocked by 0.1  $\mu$ M nafamostat (Fig 3a), which indicates that  
166 more than 0.1  $\mu$ M nafamostat may be used to investigate the existence of the TMPRSS2-  
167 dependent surface entry pathways in other cells. Consequently, 1  $\mu$ M marimastat, 25  $\mu$ M  
168 E-64d, and 10  $\mu$ M nafamostat were used to elucidate the patterns of the entry pathways  
169 in various cells. Marimastat significantly inhibited the pseudovirus entry into VeroE6  
170 (African green monkey kidney), HEC50B (human endometrium), OVTOKO (human  
171 ovary), and A704 cells (Fig 3b). In addition to the metalloproteinase pathway, virus entry  
172 was partially inhibited by E-64d, and the combination of marimastat and E-64d showed  
173 additive effects in VeroE6, HEC50B, and OVTOKO cells (Fig 3b). These results suggest  
174 that the metalloproteinase and endosomal pathways are mutually independent. Neither

175 marimastat nor nafamostat alone significantly inhibited the entry pathways of IGROV1  
176 (human ovary), OUMS-23 (human colon), or OVISE, whereas E-64d significantly  
177 inhibited the entry pathways of IGROV1 and OUMS-23 cells and the overall entry  
178 pathway into the OVISE cells (Fig 3c). Interestingly, E-64d resistant entry in IGROV1  
179 cells was inhibited by the combination of marimastat with E-64d while the E-64d resistant  
180 entry into OUMS-23 cells was inhibited by the combination of nafamostat and E-64d.  
181 These results indicate that the endosome entry pathway dominates these cells, while  
182 coexisting with either the metalloproteinase or TMPRSS2 surface pathway. Nafamostat  
183 inhibited the overall entry pathways into the Calu-3 and Caco-2 (human colon) cells,  
184 while marimastat and E-64d showed no inhibitory effects. (Fig 3d). Together, these  
185 findings show that the metalloproteinase-dependent cell surface entry pathway exists in  
186 a cell type-dependent manner and coexists with the endosome pathway in some cell lines.  
187 As we could not find cell lines with both metalloproteinase- and TMPRSS2-dependent  
188 cell surface entry pathways, we generated HEC50B cell lines ectopically expressing  
189 TMPRSS2 (HEC50B-TMPRSS2). In the HEC50B-TMPRSS2 cells, approximately 80%  
190 of the entry pathways were TMPRSS2-dependent, while the rest were predominantly  
191 metalloproteinase-dependent (Fig 3e). This indicates that the metalloproteinase pathway

192 independently coexists with the TMPRSS2 dependent pathway. These results also  
193 suggest that there could be cells *in vivo* that naturally have both surface entry pathways.

194

195 **The metalloproteinase pathway requires both the furin-cleavage site and S2 region**  
196 **of the SARS-CoV-2 S protein**

197 Our results showed that metalloproteinase-dependent and TMPRSS2-independent cell-  
198 cell fusion was induced by the S protein of SARS-CoV-2 but not by that of SARS-CoV  
199 or MERS-CoV (Fig 1a,b). In line with these results, metalloproteinase-dependent entry  
200 was observed only when the pseudovirus bearing the S protein of SARS-CoV-2, but not  
201 SARS-CoV or MERS-CoV, was used in HEC50B (Fig 4a), A704 (S4a Fig), and VeroE6  
202 cells (S4b Fig). Furthermore, pseudoviruses bearing the S protein of HCoV-NL63 and  
203 WIV1-CoV, which like SARS-CoV-2 use ACE2 as their receptor, cannot utilize the  
204 metalloproteinase pathway in HEC50B cells (Fig 4b). While SARS-CoV-2 S uses both  
205 the metalloproteinase and endosome pathways, SARS-CoV, MERS-CoV, HCoV-NL63,  
206 and WIV1-CoV S exclusively use the endosome pathway, and none of these S proteins  
207 can use the metalloproteinase or TMPRSS2 pathway in HEC50B (Fig 4a,b), A704 (S4a  
208 Fig), and VeroE6 cells (S4b Fig). The ability to use the metalloproteinase pathway and

209 sensitivities against various protease inhibitors are conserved among the variants of  
210 SARS-CoV-2 we tested (S5 Fig).

211           The S proteins of SARS-CoV-2 and MERS-CoV have furin cleavage sites (Arg-  
212 X-X-Arg) in their S1/S2 boundary area, and they were efficiently cleaved during the  
213 preparation of the pseudovirus (Fig 4c,d). In contrast, the S proteins of SARS-CoV,  
214 HCoV-NL63, and WIV1-CoV, which do not use the metalloproteinase pathway, do not  
215 have furin cleavage site and are not cleaved to any notable degree (Fig 4c,d and S6 Fig).  
216 Given that the MERS-CoV S protein does not use the metalloproteinase pathway (Fig 4a)  
217 even though it harbors a furin cleavage site and was efficiently cleaved, we speculated  
218 that furin-catalyzed S protein cleavage is a prerequisite but not sufficient for using the  
219 metalloproteinase pathway. To test this hypothesis, we generated pseudoviruses bearing  
220 chimeric S proteins in which the S1, S1/S2 boundary, and S2 domains were derived from  
221 either SARS-CoV or SARS-CoV-2 (Fig 4c,d). As expected, the S2 fragment of the C-  
222 terminal Flag-tagged S protein was mainly detected with anti-Flag antibody when  
223 pseudoviruses bearing S proteins with the furin-cleavage site (S121, S122, SARS-CoV-  
224 2 S (222), and S221) were analyzed (Fig 4d). In contrast, uncleaved S protein (S0) was  
225 mainly detected when S proteins without the furin-cleavage site (SARS-CoV S (111),  
226 S112, S212, and S211) were used (Fig 4d). When only section, the S1/S2 boundary or the

227 S2 domain, was replaced with the corresponding domain of SARS-CoV-2 in the SARS-  
228 CoV S protein (S121, S112), the metalloproteinase pathway did not appear (Fig 4e).  
229 However, when both the S1/S2 and S2 domains were replaced with the corresponding  
230 domains of SARS-CoV-2 (S122), the metalloproteinase pathway appeared in addition to  
231 the endosome pathway (Fig 4e), similar to the pattern observed for bona fide SARS-CoV-  
232 2 S (S222) (Fig 4f). Furthermore, when either the S1/S2 or S2 domain was replaced with  
233 the corresponding domain of SARS-CoV in the SARS-CoV-2 S protein (S212, S221), the  
234 metalloproteinase pathway disappeared (Fig 4f). Similar requirements for the S1/S2  
235 boundary and S2 domains for SARS-CoV-2 to use the metalloproteinase pathway were  
236 also observed in VeroE6 cells (S4c,d Fig). These results indicate that both the S1/S2  
237 boundary and S2 domain of SARS-CoV-2 are strictly required for the virus to utilize the  
238 metalloproteinase pathway when the endosome pathway coexists.

239 To compare the structural requirements needed for the S protein to use the  
240 metalloproteinase pathway with those needed to use the TMPRSS2 pathway in cells with  
241 the endosome pathway as an alternative, we used HEC50B-TMPRSS2 and VeroE6 cells  
242 ectopically expressing TMPRSS2 (VeroE6-TMPRSS2). While both these cell types  
243 exhibit the TMPRSS2 and endosome pathways depending on the source of S protein (Fig  
244 4g and S4e Fig), HEC50B-TMPRSS2 cells in addition maintained a significant amount

245 of the metalloproteinase pathway (approximately 20% of the total entry pathway) (Fig  
246 3e), whereas most of the metalloproteinase pathway disappeared in the VeroE6-  
247 TMPRSS2 cells when compared with their parental line (Fig 3b and S4e Fig). Given that  
248 the metalloproteinase pathway is dependent on the structural features of the S protein, its  
249 blockade by marimastat will promote protein structural requirements for S protein to use  
250 the TMPRSS2 pathway in HEC50B-TMPRSS2 (Fig 4g-i) but not in VeroE6-TMPRSS2  
251 cells (S4e-g Fig). In both cell types, SARS-CoV-2 predominantly used the TMPRSS2  
252 entry pathway, while SARS-CoV used the endosome pathway (Fig 4g and S4e Fig).  
253 However, nafamostat partially, but more efficiently, inhibited the entry of S112 and S121  
254 pseudoviruses when compared with SARS-CoV (S111), while it inhibited S122 virus  
255 entry almost completely (Fig 4h and S4f Fig). Furthermore, when compared with SARS-  
256 CoV-2 (S222), nafamostat only partially inhibited S221 or S212 virus entry, while it  
257 scarcely inhibited S211 virus entry (Fig 4i and S4g Fig). These results indicate that the  
258 S1/S2 boundary and S2 domain of SARS-CoV-2 additively contribute to the ability of  
259 the virus to use the TMPRSS2 pathway. Together, these results show that although both  
260 the TMPRSS2 and the metalloproteinase pathways undergo priming of the S protein at  
261 the cell surface, the structural requirements of the S protein for efficient priming differ  
262 between the metalloproteinase and TMPRSS2 pathways.

263

264 **Possible involvement of ADAM-10 in the metalloproteinase-dependent entry of**  
265 **SARS-CoV-2**

266 In addition to marimastat, other metalloproteinase inhibitors, including prinomastat,  
267 ilomastat, and CTS-1027, which block the TMPRSS2-independent cell-cell fusion  
268 induced by SARS-CoV-2 S (Fig 2b), inhibited the metalloproteinase-dependent entry of  
269 SARS-CoV-2 pseudovirus in VeroE6, HEC50B, and A704 cells (Fig 5a). Since these  
270 inhibitors exhibited broad specificity[30-33], selective inhibitors were then used to  
271 narrow down the metalloproteinases involved in the metalloproteinase-dependent entry  
272 pathway. The VeroE6 and HEC50B cells had significantly E-64d sensitive endosome  
273 pathways but the A704 cells did not (Fig 3b). Consequently, selective metalloproteinase  
274 inhibitors were tested in the presence of E-64d so that the reduction in the  
275 metalloproteinase pathway could be easily recognized in VeroE6 and HEC50B cells (Fig  
276 5a). Similar inhibitory patterns were observed in all three cell lines tested (Fig 5a), and  
277 their viabilities were not affected by any of the metalloproteinase inhibitors at the  
278 concentrations used in the experiment (S7a-d Fig). These results suggest that the  
279 metalloproteinases involved in the pathway are likely to be common to all three cell lines.  
280 GW280264X[34] (ADAM10/17 inhibitor) and GI1254023X[34, 35] (MMP9/ADAM10



281 inhibitor) significantly inhibited the metalloproteinase pathway, whereas TAPI2[36]  
282 (ADAM-17 inhibitor) and BK-1361[37] (ADAM8 inhibitor) did not (Fig 5a). This  
283 suggests that ADAM10 may be involved in the ADAM family. MMP408[30]  
284 (MMP3/12/13 inhibitor) and MMP2/9 inhibitor I[38] scarcely affected virus entry,  
285 whereas UK370106[39] (MMP3/12 inhibitor) and MMP9 inhibitor I[40] were  
286 significantly inhibitory (Fig5a), suggesting that MMP3/9/12/13 may not be crucial, but  
287 that the unidentified metalloproteinase, which could be inhibited by UK370106 or MMP9  
288 inhibitor I, may be involved in the pathway in cooperation with ADAM10. MLN-  
289 4760[41] (ACE2 inhibitor) did not inhibit virus entry (Fig 5a), indicating that the catalytic  
290 activity of ACE2, to which the S protein directly binds as a receptor, is not involved. To  
291 further confirm the involvement of ADAM10 in the metalloproteinase-dependent  
292 pathway, ADAM10 was depleted by siRNA in HEC50B cells. Three independent siRNAs  
293 effectively suppressed the expression of both the precursor and active forms of ADAM10  
294 (Fig 5b). An ADAM10 knockdown significantly inhibited SARS-CoV-2 pseudovirus  
295 entry, while the entry of SARS-CoV, MERS-CoV, and VSVG pseudoviruses were not  
296 affected (Fig 5c), indicating that ADAM10 plays a role unique to SARS-CoV-2 in viral  
297 entry. Furthermore, we examined the effects of the ADAM10 knockdown on the entry  
298 pathway patterns by treating siRNA-transfected cells with either E-64d, marimastat, or a

299 combination of both. The combination treatment with E-64d and marimastat led to an  
300 additive effect for the single treatments, resulting in the complete inhibition of viral entry  
301 in both cells with normal ADAM10 expression and those with reduced ADAM10  
302 expression (Fig 5d). These results indicated that E-64d-resistant viral entry is a  
303 metalloproteinase-dependent pathway, while marimastat-resistant viral entry is  
304 dependent on the endosome pathway. The ADAM10-knockdown significantly inhibited  
305 the metalloproteinase pathway (Fig 5e, E64-d treatment) while the ADAM10-knockdown  
306 had only a modest effect on the endosome pathway (Fig 5e, marimastat-treatment),  
307 indicating that ADAM10 is involved in the metalloproteinase-dependent entry pathway  
308 of SARS-CoV-2.

309         Recently, it was reported that ACE2 shedding by ADAM17 promotes SARS-  
310 CoV-2 infection[42]. While a CRISPR/Cas9-mediated knockout of ADAM17 enhanced  
311 the accumulation of cellular ACE2 in HEC50B cells due to the inhibition of ACE2  
312 shedding (S8a Fig), SARS-CoV-2 S pseudovirus entry was increased, and this was  
313 probably because of the enhanced binding of virus to the cell surface ACE2 (S8b Fig).  
314 However, the patterns of the metalloproteinase and endosome pathways were similar  
315 between the wild-type and ADAM17 knockout cells (S8c Fig), suggesting that ADAM17  
316 may not be involved in metalloproteinase-dependent virus entry in HEC50B cells.

317

318 **The metalloproteinase-dependent entry pathway of authentic SARS-CoV-2 is**  
319 **involved in syncytia formation and cytopathicity**

320 To confirm the involvement of the metalloproteinase pathway in authentic SARS-CoV-2  
321 entry, we first evaluated the effects of marimastat and prinomastat on the amount of  
322 cytoplasmic viral RNA transcribed from the N gene after infection. Both inhibitors  
323 significantly suppressed SARS-CoV-2 infection (Fig 6a). The IC<sub>50</sub> values of the  
324 marimastat and prinomastat were 160 nM and 130 nM in HEC50B cells, and 150 nM and  
325 250 nM in the A704 cells, respectively. The IC<sub>50</sub> value of the marimastat in the VeroE6  
326 cells was 340 nM. Consistent with the results from the pseudoviruses experiments,  
327 nafamostat showed a marked inhibitory effect on the Calu-3 cells but not on the HEC50B,  
328 A704, or VeroE6 cells (S9a Fig). In contrast, 25 μM E-64d and 10 mM NH<sub>4</sub>Cl, which  
329 inhibits endosome-lysosome system acidification[43], significantly suppressed SARS-  
330 CoV-2 infection in the HEC50B, A704, and VeroE6 cells (S9b,c Fig). This indicated that  
331 the endosome pathway coexists with the metalloproteinase pathway to contribute to  
332 authentic SARS-CoV-2 infection in these cells. Combination treatments with E-  
333 64d/marimastat or NH<sub>4</sub>Cl/marimastat showed much stronger inhibitory effects than the  
334 treatment with each drug alone (Fig 6b). Similarly, combination treatments with

335 nafamostat and marimastat or nafamostat and E-64d showed stronger inhibitory effects  
336 than the nafamostat treatment alone in the HEC50B-TMPRSS2 cells (Fig 6c).  
337 Furthermore, when all three drugs were combined, they had a much stronger inhibitory  
338 effect on viral infection when compared with the two-drug combinations (Fig 6c). These  
339 results strongly suggest that drugs that block the metalloproteinase pathway are effective  
340 for COVID-19 treatment.

341         Next, we examined whether ADAM10 is involved in SARS-CoV-2 infection.  
342 GW280264X[34] (ADAM10/17 inhibitor) and GI1254023X[34, 35] (MMP9/ADAM10  
343 inhibitor) significantly suppressed SARS-CoV-2 infection, whereas TAPI2[36] (ADAM-  
344 17 inhibitor) did not (Fig 6d). Moreover, the ADAM10 knockdown by siRNA suppressed  
345 SARS-CoV-2 infection by approximately 40% (Fig 6e), indicating that ADAM10 is  
346 partially involved. This effect was smaller than that for the various metalloproteinase  
347 inhibitors (Fig 6a,d), suggesting that metalloproteinases other than ADAM10 are also  
348 involved in this pathway.

349         The ability of SARS-CoV-2 to form syncytia and induce cytopathicity is thought  
350 to be related to its pathogenesis[44, 45]. To determine whether the metalloproteinase-  
351 dependent pathway is involved in syncytia formation, we first used HEC50B cells as a  
352 representative for cells that predominantly use the metalloproteinase and endosome

353 pathways. Interestingly, the SARS-CoV-2-induced syncytia formation in HEC50B cells  
354 24 h after infection was significantly blocked by 500 nM of marimastat and prinomastat  
355 but not notably affected by 25  $\mu$ M E-64d (Fig 6f and S10 Fig). These results indicate that  
356 the metalloproteinase-dependent pathway, but not the endosome pathway, is crucial for  
357 syncytium formation, although both pathways similarly reduce viral infection (Fig 6b).  
358 Given that the metalloproteinases are normally localized at the cell surface, we used  
359 HEC50B-TMPRSS2 cells, which have cell surface TMPRSS2 and metalloproteinase  
360 pathways, to investigate their involvement in syncytia formation when they coexist. The  
361 SARS-CoV-2-induced syncytia formation in the HEC50B-TMPRSS2 cells was not  
362 significantly inhibited by marimastat or nafamostat alone, but was clearly inhibited by  
363 the combined treatment (Fig 6g). These results suggest that the metalloproteinase and  
364 TMPRSS2 pathways cooperate to form syncytia. Next, we addressed the role of the  
365 metalloproteinase pathway in SARS-CoV-2-induced cytotoxicity. SARS-CoV-2-induced  
366 cytopathicity of HEC50B cells 3 d after infection was not inhibited by either E-64d,  
367 marimastat, or prinomastat alone, but was significantly blocked when cells were treated  
368 with E-64d in combination with either marimastat or prinomastat (Fig 6h). In addition,  
369 SARS-CoV-2-induced cytopathicity of the HEC50B-TMPRSS2 cells was not inhibited  
370 by either E-64d, nafamostat, or marimastat alone, but was significantly blocked when

371 cells were treated with a combination of all three drugs (Fig 6i). These results strongly  
372 suggest that the inhibition of the metalloproteinase pathway is crucial to block syncytia  
373 formation and cytopathicity *in vivo*, and consequently, that the metalloproteinase pathway  
374 is likely to be involved in the pathogenesis of COVID-19.

375

## 376 **Discussion**

377 Previous studies of the S proteins found in SARS-CoV-2, SARS-CoV, and MERS-CoV  
378 have shown that the priming of the S2 domain, catalyzed by either TMPRSS2 on the  
379 plasma membrane or cathepsin-B/L in endosomes, results in the fusion peptide protruding  
380 to induce envelope fusion, thereby establishing viral entry through the plasma membrane  
381 or endosomal membrane, respectively[14, 19, 20]. In this study, we have demonstrated  
382 that SARS-CoV-2, unlike SARS-CoV or MERS-CoV, has a unique TMPRSS2-  
383 independent cell surface entry pathway, which is sensitive to various metalloproteinase  
384 inhibitors including ilomastat, CTS-1027, marimastat, and prinomastat, but resistant to  
385 previously known inhibitors of SARS-CoV-2 entry, such as nafamostat[24, 46] and E-  
386 64d[19]. As a representative of these broad-spectrum metalloproteinase inhibitors, we  
387 chose marimastat to investigate the cell type-dependent distribution of the  
388 metalloproteinase pathway by measuring pseudovirus infection. A significant proportion

389 of the entry pathway is metalloproteinase-dependent in A704 (kidney), HEC50B  
390 (endometrium), OVTOKO (ovary), and VeroE6 (kidney) cells. Only a small proportion  
391 was metalloproteinase-dependent in IGROV1 (ovary) cells, while the metalloproteinase  
392 pathway was not detected in OMUS-23 (colon), OVISE (ovary), Calu-3 (lung), and Caco-  
393 2 (colon) cells. These results indicate that the metalloproteinase pathway of SARS-CoV-  
394 2 is cell-type specific and independently coexists with other entry pathways, including  
395 the TMPRSS2-dependent surface pathway and the endosome pathway. The kidney[47,  
396 48], ovary[49, 50], and endometrium[51] are known to express ACE2. Furthermore,  
397 SARS-CoV-2 can infect the kidney[48, 52] and induce acute kidney injury[53] in  
398 COVID-19 patients. Although SARS-CoV-2 infection of the ovary or endometrium has  
399 not previously been reported, the metalloproteinase-dependent infection pathway may  
400 contribute to the pathogenesis of COVID-19, especially multiple organ failure. The  
401 metalloproteinase pathway is thus a potential target for future COVID-19 therapies.

402         The S1/S2 boundary of SARS-CoV-2 contains the furin cleavage motif (Arg-X-  
403 X-Arg), while that of SARS-CoV contains only a single Arg. It has been reported that the  
404 motif greatly increases the efficiency of S1/S2 cleavage[15, 16], leading to enhanced viral  
405 transmission both *in vitro*[15, 16, 23] and *in vivo*[54, 55]. This may be partially due to  
406 the enhanced availability of S2 to TMPRSS2, due to the dissociation of S1[56, 57]. We

407 have shown that the furin cleavage motif is required for the metalloproteinase pathway,  
408 and we propose that the induction of metalloproteinase-induced S2 priming is another  
409 role of furin-mediated S1/S2 cleavage in enhanced viral transmission. Therefore, the  
410 metalloproteinase-dependent entry pathway, which is unique among highly pathogenic  
411 coronaviruses, is likely to be associated with the rapid spread of SARS-CoV-2.  
412 Interestingly, experiments using pseudoviruses bearing chimeric S proteins between  
413 SARS-CoV (without the metalloproteinase pathway) and SARS-CoV-2 (with the  
414 metalloproteinase pathway) revealed that both the S1/S2 boundary of SARS-CoV-2 and  
415 the S2 domain of SARS-CoV-2 S are essential for metalloproteinase-dependent entry. In  
416 contrast, the two domains of SARS-CoV-2 independently contributed to TMPRSS2-  
417 dependent S2 priming. This discrepancy may be partially due to the difference in the  
418 substrate recognition properties of the priming proteases in the two pathways. The S112  
419 pseudovirus (a VSV pseudovirus bearing SARS-CoV S mutant, in which the S2 region  
420 was replaced with the corresponding domain of SARS-CoV-2) can use the TMPRSS2  
421 pathway more efficiently than the SARS-CoV S pseudovirus, which suggests that  
422 TMPRSS2 may be partially accessible to the priming site in SARS-CoV-2 (C-terminal of  
423 Arg815) but not to that in SARS-CoV (C-terminal of Arg797) without S1 dissociation.  
424 In contrast, the putative priming protease in the metalloproteinase pathway, which may



425 not be a metalloproteinase but a protease activated by metalloproteinases, can access the  
426 priming site only when the site occurs within the contextual characteristics of SARS-  
427 CoV-2 S2, and S1/S2 is cleaved to allow S1 dissociation. Determination of the priming  
428 site in the metalloproteinase pathway and identification of the critical amino acid residues  
429 generating the structural characteristics of SARS-CoV-2 S2 that allow metalloproteinase-  
430 dependent priming are required to understand its molecular mechanisms for the two  
431 distinct surface entry pathways. From an evolutionary perspective, SARS-CoV-2  
432 acquired the metalloproteinase pathway by introducing mutations into the S2 region,  
433 which may have contributed to the SARS-CoV-2 pandemic. The function of point  
434 mutations in the S2 domain have not yet been fully analyzed in comparison to those in  
435 the S1 domain, which cause escape from neutralizing antibodies[58]. However, various  
436 point mutations in the S2 domain may play important roles in increasing the efficiency of  
437 infection and disease progression and the generation of highly infectious variants.

438         Using selective metalloproteinase inhibitors and ADAM10 knockdowns  
439 generated using specific siRNAs, we have demonstrated that ADAM10 plays an  
440 important role in the metalloproteinase pathway. ADAM10 is ubiquitously expressed in  
441 various tissues[59] and cell lines[60], and functionally regulates cell differentiation and  
442 proliferation by cleaving ligands and receptors such as epidermal growth factor (EGF),

443 heparin-binding EGF-like growth factor (HB-EGF), and Notch[61]. ADAM10 is thus  
444 likely to contribute to SARS-CoV-2 infection in various organs. ADAM17, similar to  
445 ADAM10, is also known as a metalloproteinase that induces the cleavage of receptors  
446 and ligands, and both can cleave common substrates such as Notch and HB-EGF[61]. It  
447 has been reported that ACE2 shedding by ADAM17 promotes SARS-CoV-2  
448 infection[42]. Although we observed that ADAM17 depletion resulted in the cellular  
449 accumulation of ACE2, which is indicative of reduced ACE2 shedding, total SARS-CoV-  
450 2 pseudovirus infection was unexpectedly augmented and the relative contribution of the  
451 metalloproteinase pathway was not affected. ADAM10 and ADAM17 thus both play  
452 crucial but distinct roles in SARS-CoV-2 infection. It has recently been reported that  
453 ADAM9 inhibition decreases SARS-CoV-2 infection *in vitro*[62]. Although the  
454 involvement of ADAM9 in viral entry is not clear, the results suggest that a group of  
455 metalloproteinases cooperate in the metalloproteinase pathway. This may indicate that  
456 the observed ADAM10 depletion-induced inhibition was a part of the maximum  
457 inhibition by various metalloproteinase inhibitors. A recent report also showed that  
458 MMP12 knockouts inhibited SARS-CoV-2 infection *in vitro*[63]. However,  
459 MMP408[30], an inhibitor of MMP12, did not prevent SARS-CoV-2 infection in various  
460 cell lines in this investigation, suggesting that metalloproteinases involved in the

461 metalloproteinase pathway may differ in a cell type-dependent manner. Further studies  
462 are required to identify the functional metalloproteinases that are involved in the  
463 metalloproteinase pathway.

464         Various compounds are reported to inhibit SARS-CoV-2 infection by inhibiting  
465 envelope fusion *in vitro*. However, camostat[64], an inhibitor of the TMPRSS2-  
466 dependent surface entry, and hydroxychloroquine[65, 66], an inhibitor of the endosomal  
467 pathway, have failed to show sufficient therapeutic efficacy in clinical trials. Our entry  
468 pathway analysis revealed that the metalloproteinase surface pathway coexists with the  
469 TMPRSS2 pathway and/or the endosome pathway in various cell types. Furthermore, in  
470 HEC50B and HEC50B-TMPRSS2 cells, cell death could not be inhibited unless all entry  
471 pathways in each cell were inhibited using inhibitor co-treatments for each pathway.  
472 Therefore, future clinical trials on virus entry in which the TMPRSS2, metalloproteinase,  
473 and endosome pathways are all efficiently blocked, need to be conducted. We propose  
474 that to address this challenge both marimastat and prinomastat should be utilized in  
475 clinical trials. The mean maximum plasma concentration ( $C_{max}$ ) at a reasonably well-  
476 tolerated dose was 590 nM for marimastat[27] and 680 nM for prinomastat[28].  
477 Furthermore, we demonstrated that these two drugs significantly inhibited SARS-CoV-2  
478 infection at concentrations lower than their  $C_{max}$  values. These metalloprotease inhibitors,

479 in combination with other protease inhibitors targeting the TMPRSS2 and endosome  
480 pathways, may effectively inhibit SARS-CoV-2 infection in various tissues and cure  
481 COVID-19. Recently, there has been concern about the spread of SARS-CoV-2 variants,  
482 such as the delta strain, as they reduce the effectiveness of the neutralizing antibodies  
483 produced by vaccination[7, 9, 10]. Since sensitivities against marimastat, nafamostat, and  
484 E-64d have been conserved in the various variants investigated so far, the strategies to  
485 use protease inhibitors for COVID-19 treatment are likely to be significantly effective  
486 against these variants. The results of this study may contribute to the development of  
487 COVID-19 treatments targeting viral entry pathways.

488

## 489 **Materials and Methods**

### 490 **Cell lines, viruses, and reagents**

491 VeroE6 (CRL-1586), 293T (CRL-3216), A704 (HTB-45) and Calu-3 (HTB-55) cells  
492 were obtained from the American Type Culture Collection (Rockville, MD, USA).  
493 OVTOKO (JCRB1048), OWISE (JCRB1043), HEC50B (JCRB1145), VeroE6-  
494 TMPRSS2 (JCRB1819)[67], and OUMS-23 (JCRB1022) cells were obtained from the  
495 Japanese Collection of Research Bioresources Cell Bank (Osaka, Japan). IGROV1 cells  
496 (SCC203) were purchased from Merck (Darmstadt, Germany) and Caco-2 cells

497 (RCB0988) were obtained from the RIKEN BioResource Research Center (Tsukuba,  
498 Japan). A704, Calu-3, VeroE6, HEC50B, and Caco-2 cells were maintained in Eagle's  
499 minimum essential medium (EMEM; 055-08975, FUJIFILM Wako Pure Chemical,  
500 Osaka, Japan) containing 15% fetal bovine serum (FBS). OUMS-23, IGROV1, and 293T  
501 cells were maintained in Dulbecco's modified Eagle's medium (DMEM; 041-30081,  
502 FUJIFILM Wako Pure Chemical) containing 10% FBS. VeroE6-TMPRSS2 (JCRB1819)  
503 cells were cultured in DMEM containing 10% FBS and 1 mg/mL G418. OWISE and  
504 OVTOKO cells were maintained in Roswell Park Memorial Institute (RPMI)-1640  
505 medium (189-02025, FUJIFILM Wako Pure Chemical) containing 10% FBS. A pair of  
506 previously described 293FT-based reporter cell lines that stably express individual split  
507 reporters (DSP1-7 and DSP8-11 proteins)[68] were maintained in DMEM containing  
508 10% FBS and 1  $\mu$ g/mL puromycin. To establish stable cell lines expressing the S protein  
509 of SARS-CoV, SARS-CoV-2, or MERS-CoV, recombinant pseudotype lentiviruses were  
510 produced in 293T cells with psPAX2 packaging plasmid, vesicular stomatitis virus  
511 (VSV)-G-expressing plasmid and lentiviral transfer plasmid expressing S protein. To  
512 establish stable cell lines expressing ACE2 or CD26 with TMPRSS2, recombinant  
513 pseudotype lentiviruses expressing one of the proteins were produced using 293T cells  
514 with psPAX2 packaging plasmid and VSV-G-expressing plasmid. The 293FT-derived

515 reporter cells infected with the pseudotype viruses were selected with 1 µg/mL puromycin,  
516 10 µg/mL blasticidin, and 300 µg/mL hygromycin for at least 1 week. These bulk-selected  
517 cells were used for fusion assays. To establish HEC50B cells expressing TMPRSS2  
518 (HEC50B-TMPRSS2), recombinant pseudotype lentivirus expressing TMPRSS2 was  
519 produced using 293T cells with psPAX2 packaging plasmid and VSV-G-expressing  
520 plasmid. HEC50B cells infected with pseudotype viruses were selected with 300 µg/mL  
521 hygromycin for at least 1 week. The SARS-CoV-2 isolate (UT-  
522 NCGM02/Human/2020/Tokyo)[69] was propagated in VeroE6-TMPRSS2 (JCRB1819)  
523 cells in DMEM containing 5% FBS. Titers were determined with plaque assays using  
524 VeroE6/TMPRSS2 (JCRB1819) cells. Negative control No.1 siRNA (4390843), negative  
525 control No.2 siRNA (4390846), and three distanced ADAM10-specific siRNAs were  
526 purchased from Thermo Fisher Scientific (MA, USA) The siRNA sequences used were  
527 5'-UCA CCU UGU UCU ACC AUU CCA (S1004, ADAM10#1); 5'-UAA CCU CUA  
528 AAA UCG UUG CAA (S1005, ADAM10#2); and 5'-UAC GGA UUC CGG AGA AGU  
529 CTG (S1006, ADAM10#3) for the ADAM10 knockdown. Cell viability was analyzed  
530 using the CellTiter-Glo luminescent cell viability assay (G7570, Promega, WI, USA)  
531 according to the manufacturer's protocol.  
532

533 **Protease inhibitors and compound libraries**

534 Nafamostat mesylate (N0959, Tokyo Chemical Industry, Tokyo, Japan), pepstatin A  
535 (4397, Peptide institute, Osaka, Japan), bestatin (027-14101, FUJIFILM Wako Pure  
536 Chemical), leupeptin (4041, Peptide institute), E-64d (4321-v, Peptide institute), furin  
537 inhibitor II (344931, Merck), ilomastat (HY-15768, MedChemExpress, NJ, USA), CTS-  
538 1027 (HY-10398, MedChemExpress), marimastat (HY-12169, MedChemExpress),  
539 prinomastat hydrochloride (PZ0198, Sigma-Aldrich, MO, USA), UK370106 (2900,  
540 Tocris, MN, USA), GW280264X (31388, Cayman, MI, USA), GI254023X (SML0789,  
541 Sigma-Aldrich), TAPI-2 (14695, Cayman), MLN-4760 (530616, Merck), BK-1361 (PC-  
542 60981, ProbeChem, Shanghai, China), MMP408 (444291, Millipore, MA, USA),  
543 MMP2/9 inhibitor I (ab145190, Abcam, Cambridge, UK), and MMP9 inhibitor I (444278,  
544 Millipore) were dissolved in dimethyl sulfoxide (DMSO) at a concentration of 10 mM.  
545 Validated Compound Library (1,630 clinically approved compounds and 1,885  
546 pharmacologically active compounds) obtained from the Drug Discovery Initiative (The  
547 University of Tokyo) was used for compound screening.

548

549 **Expression vector construction**

550 To construct expression vectors for ACE2, CD26, and TMPRSS2, genes were cloned into  
551 a lentiviral transfer plasmid (CD500B-1, SBI, Palo Alto, CA, USA). Synthetic DNA  
552 corresponding to the codon-optimized S gene of SARS-CoV-2 (Wuhan-Hu-1, RefSeq:  
553 NC\_045512.2), SARS-CoV-2 variants (B.1.1.7, GISAID: EPI\_ISL\_601443, B.1.351,  
554 GenBank: MZ747297.1, B.1.617.1, GISAID: EPI\_ISL\_1704611, B.1.617.2, GISAID:  
555 EPI\_ISL\_3189054), SARS-CoV (Tor2, RefSeq: NC\_004718.3), bat SARS-like  
556 coronavirus WIV1 (GenBank: KF367457.1), human coronavirus NL63 (RefSeq:  
557 NC\_005831.2), and the chimeric S gene (S1, S1/S2 boundary, and S2 domains were  
558 derived from either SARS-CoV Tor2 or SARS-Cov-2 Wuhan-Hu-1), and the DNA  
559 sequence corresponding to the Flag-tag 5'-GGA GGC GAT TAC AAG GAT GAC GAT  
560 GAC AAG TAA-3' (underline, Flag-tag) at the 3' end were all generated by Integrated  
561 DNA Technologies (IA, USA). Previously described synthetic DNA corresponding to the  
562 codon-optimized S gene of a MERS-CoV (EMC 2012, RefSeq: NC\_019843.3)[25] with  
563 a DNA sequence corresponding to the Flag-tag 5'-GGA GGC GAT TAC AAG GAT  
564 GAC GAT GAC AAG TAA-3' at the 3' end was used in this study. To construct  
565 expression vectors for the S protein, the coding regions were cloned into a lentiviral  
566 transfer plasmid (CD500B-1, SBI).

567



568 **DSP assay to monitor membrane fusion**

569 DSP1-7 has the structure RL<sub>1-155</sub>-Ser-Gly-Gly-Gly-Gly-GFP<sub>1-156</sub>, while DSP8-11 has the  
570 structure Met-GFP<sub>157-231</sub>-Gly-Gly-Gly-Gly-Ser- RL<sub>156-311</sub>. RL and GFP become active  
571 only when DSP1-7 associates with DSP-8-11 (S1c Fig). For the DSP assay using 293FT  
572 cells, DSP8-11 expressing effector cells expressing S protein and DSP1-7 expressing  
573 target cells expressing CD26 or ACE2 alone or together with TMPRSS2 were seeded in  
574 10 cm cell culture plates ( $4 \times 10^6$  cells/10 mL) one day prior to the assay (S1a,b Fig).  
575 Cells were treated with 6  $\mu$ M EnduRen (Promega), a substrate for Renilla luciferase (RL),  
576 for 2 h to activate EnduRen. For compound library screening, 0.25  $\mu$ L of each compound  
577 dissolved in DMSO were added to the 384-well plates (Greiner Bioscience,  
578 Frickenhausen, Germany). To test the effects of the selected inhibitors, 1  $\mu$ L of each  
579 inhibitor dissolved in DMSO was added to the 384-well plates (Greiner Bioscience). Next,  
580 50  $\mu$ L of each single cell suspension (effector and target cells) was added to the 384-well  
581 plates using a Multidrop dispenser (Thermo Fisher Scientific, MA, USA). After  
582 incubation at 37 °C in 5% CO<sub>2</sub> for 4 h, the RL activity was measured using a Centro  
583 xS960 luminometer (Berthold, Bad Wildbad, Germany).

584

585 **Western blotting**

586 Western blot analysis was performed as described previously[70]. The primary antibodies  
587 used were rabbit anti-ACE2 (1:1000, ab15348, Abcam), rabbit anti-TACE (1:1000,  
588 3976S, Cell Signaling Technology, MA, USA), rabbit anti-ADAM10 (1:1000, 14194S,  
589 Cell Signaling Technology), rabbit anti-Flag-tag (1:1000, PM020, MBL, MA, USA),  
590 mouse anti-tubulin (1:1000, CP06, Millipore), and mouse anti-VSV (1:1000, 23H12,  
591 Absolute antibody). The Secondly antibodies used were HRP-linked donkey anti-rabbit  
592 IgG antibody (NA934; GE Healthcare, Piscataway, NJ, USA) and HRP-linked donkey  
593 anti-mouse IgG antibody (NA931V; GE Healthcare). Cell supernatants containing the  
594 pseudotype viral particles were centrifuged at 109,000 g or 35 min at 4 °C using a  
595 TLA100.3 rotor with an Optima TLX ultracentrifuge (Beckman Coulter, CA, USA), and  
596 the pellet was then lysed for western blotting analysis.

597

### 598 **Preparation of pseudotype VSV viral particles and infection experiments**

599 To prepare pseudotype VSV viral particles 293T cells were transfected with an expression  
600 plasmid for S, VSV G, or a control expression plasmid using calcium phosphate  
601 precipitation. At 16 h post-transfection, the cells were inoculated with a replication-  
602 deficient VSV,  $\Delta$  VSV-Luci, which lacks the VSV G gene and encodes firefly luciferase,  
603 at a multiplicity of infection (MOI) of 1, as was described previously[71]. After

604 incubation at 37 °C in 5% CO<sub>2</sub> for 2 h, the cells were washed with DMEM and further  
605 incubated at 37 °C in 5% CO<sub>2</sub> for 16 h before the supernatants containing the pseudotype  
606 viral particles were harvested. Cellular debris was removed from the supernatants using  
607 a syringe filter with a 0.45 µm size pore (Millipore). For the infection assay, target cells  
608 were seeded in 96-well plates (2 × 10<sup>4</sup> cells/well) and incubated overnight at 37 °C with  
609 5% CO<sub>2</sub>. The cells were pre-treated with inhibitors for 1 h before infection. Pseudotype  
610 viral particles were added to the cells in the presence of the inhibitors. Luciferase activity  
611 was measured 16 h post-infection using the Bright-Glo Luciferase Assay System or ONE-  
612 Glo Luciferase Assay System (Promega) and Centro xS960 luminometer (Berthold).

613

#### 614 **Transfection**

615 siRNA transfection was performed using Lipofectamine RNAiMAX (Thermo Fisher  
616 Scientific) according to the manufacturer's protocol. Cells were seeded in 6-well plates  
617 (1.6 × 10<sup>6</sup> cells/well) with siRNA and Lipofectamine RNAiMAX. Then 24 h after  
618 transfection, the cells were seeded in 96-well plates (2 × 10<sup>4</sup> cells/well), and 48 h after  
619 transfection the cells were used for the infection experiments.

620

#### 621 **Quantification of intracellular SARS-CoV-2 RNA**

622 Cells were seeded at  $5 \times 10^4$  cells per well in a 96-well cell culture plate. After an  
623 overnight incubation at 37 °C in 5% CO<sub>2</sub>, cells were treated with protease inhibitors for  
624 1 h and added with SARS-CoV-2 at a multiplicity of infection (MOI) of 0.01 for HEC50B  
625 and HEC50B-TMPRSS2 cells, and MOI of 0.1 for VeroE6, Calu-3, and A704 cells. After  
626 24 h of incubation at 37 °C in 5% CO<sub>2</sub>, the cells were washed three times with PBS. Cell  
627 lysis and cDNA synthesis were performed using SuperPrep II Cell Lysis & RT Kit for  
628 qPCR (SCQ-401, TOYOBO, Osaka, Japan) following the manufacturer's instructions.  
629 SARS-CoV-2 RNA was detected using a primer set targeting the SARS-CoV-2 N gene.  
630 Quantitative real-time RT-PCR was performed using THUNDERBIRD SYBR qPCR  
631 Mix (TOYOBO) at 95 °C for 3 min, followed by 50 cycles of 95 °C for 10 s and 60 °C  
632 for 1 min. Fluorescence was detected during the thermal cycling process, and  
633 quantification studies were performed using the CFX Connect™ Real-Time PCR  
634 detection system (Bio-Rad, CA, USA). The level of ribosomal protein L13a (*Rpl13a*)  
635 mRNA expression in each sample was used to standardize the data. The primer sequences  
636 used were 5'-AAA TTT TGG GGA CCA GGA AC-3' (forward primer) and 5'-TGG CAG  
637 CTG TGT AGG TCA AC-3' (reverse primer) for the SARS-CoV-2 N gene; 5'-TGT TTG  
638 ACG GCA TCC CAC-3' (forward primer) and 5'-CTG TCA CTG CCT GGT ACT TC-  
639 3' (reverse primer) for human *Rpl13a* gene; and 5'-CTC AAG GTT GTG CGT CTG AA-

640 3' (forward primer) and 5'-CTG TCA CTG CCT GGT ACT TCC A-3' (reverse primer)

641 for the African green monkey *Rpl13a* gene.

642

### 643 **Immunofluorescence Staining**

644 HEC50B and HEC50B-TMPRSS2 cells were seeded at  $1.5 \times 10^5$  cells per well in a 24-

645 well cell culture plate. After an overnight incubation at 37 °C in 5% CO<sub>2</sub>, cells were

646 treated with protease inhibitors for 1 h and then with SARS-CoV-2 at an MOI of 1. After

647 24 h of incubation at 37 °C in 5% CO<sub>2</sub>, cells were fixed with 4% paraformaldehyde in

648 PBS(-) for 10 min at RT and then permeabilized with 0.1% Triton X-100 in PBS(-) for

649 10 min at RT. Cells were then incubated with anti-SARS-CoV-2 nucleocapsid (1:1000,

650 GTX135357, GeneTex, CA, USA) primary antibody for 16 h at 4 °C and detected with

651 anti-rabbit-Alexa488 (1:200, A11008, Invitrogen, CA, USA) secondary antibodies for 40

652 min at RT. Cell nuclei were stained with 1 µg/mL Hoechst 33342 (#080-09981,

653 FUJIFILM Wako Pure Chemical). Fluorescent signals were detected using a BZ-X810

654 fluorescent microscope (Keyence, Osaka, Japan).

655

### 656 **Cytopathicity assay**

657 HEC50B and HEC50B-TMPRSS2 cells were seeded at  $1.5 \times 10^5$  cells per well in a 24-  
658 well cell culture plate. After an overnight incubation at 37 °C in 5% CO<sub>2</sub>, cells were  
659 treated with protease inhibitors for 1 h and then with SARS-CoV-2 at an MOI of 1. To  
660 maintain the drug concentration, half of the culture supernatant was replaced daily with  
661 fresh medium that contained drugs. After incubation at 37 °C in 5% CO<sub>2</sub> for 3 d, the cells  
662 were fixed with 4% paraformaldehyde in PBS for 10 min at 25 °C and stained with 0.2%  
663 crystal violet solution for 5 min. After washing four times with water, the wells were air-  
664 dried at 25 °C. Ethanol was added to each well to dissolve crystal violet. The absorbance  
665 was measured at 595 nm using an iMark™ Microplate Reader (Bio-Rad).

666

#### 667 **Statistical analysis**

668 Statistical analyses were performed in Microsoft Excel 2016 (Microsoft, Redmond, WA,  
669 USA) and GraphPad Prism 8 (GraphPad Software, San Diego, CA). Statistically  
670 significant differences between the mean values were determined using a two-tailed  
671 Student's t-test. Dunnett's test and Tukey's test were used for multiple comparisons. All  
672 data represent three independent experiments, and values represent the mean  $\pm$  standard  
673 deviation (s.d.), with a  $p < 0.05$ , considered statistically significant.

674

675 **Acknowledgements**

676 We thank Yoshihiro Kawaoka for providing the SARS-CoV-2 isolate (UT-  
677 NCGM/Human/2020/Tokyo), Robert Whittier for critical reading of our manuscript and  
678 Kinuyo Miyazaki for her secretarial assistance.

679

680 **Author contributions**

681 M.Y., J.G., and J.I. designed the study; M.Y., J.G., A.K., K.T., and Y.H. performed the  
682 experiments; M.Y., J.G., N.K., M.S., K.S., T.A., Y.K., and J.I. analyzed and interpreted  
683 the data; and M.Y. and J.I. wrote the manuscript.

684

685 **References**

- 686 1. Zhou P, Yang XL, Wang XG, Hu B, Zhang L, Zhang W, et al. A pneumonia outbreak  
687 associated with a new coronavirus of probable bat origin. *Nature*. 2020;579(7798):270-3.  
688 Epub 2020/02/03. doi: 10.1038/s41586-020-2012-7. PubMed PMID: 32015507; PubMed  
689 Central PMCID: PMC7095418.
- 690 2. Zhong NS, Zheng BJ, Li YM, Poon, Xie ZH, Chan KH, et al. Epidemiology and cause  
691 of severe acute respiratory syndrome (SARS) in Guangdong, People's Republic of China, in  
692 February, 2003. *Lancet*. 2003;362(9393):1353-8. doi: 10.1016/s0140-6736(03)14630-2.

- 693 PubMed PMID: 14585636; PubMed Central PMCID: PMC7112415.
- 694 3. Drosten C, Günther S, Preiser W, van der Werf S, Brodt HR, Becker S, et al.  
695 Identification of a novel coronavirus in patients with severe acute respiratory syndrome. N  
696 Engl J Med. 2003;348(20):1967-76. Epub 20030410. doi: 10.1056/NEJMoa030747. PubMed  
697 PMID: 12690091.
- 698 4. Zaki AM, van Boheemen S, Bestebroer TM, Osterhaus AD, Fouchier RA. Isolation  
699 of a novel coronavirus from a man with pneumonia in Saudi Arabia. N Engl J Med.  
700 2012;367(19):1814-20. doi: 10.1056/NEJMoa1211721. PubMed PMID: 23075143.
- 701 5. Harrison AG, Lin T, Wang P. Mechanisms of SARS-CoV-2 Transmission and  
702 Pathogenesis. Trends Immunol. 2020;41(12):1100-15. Epub 20201014. doi:  
703 10.1016/j.it.2020.10.004. PubMed PMID: 33132005; PubMed Central PMCID:  
704 PMC7556779.
- 705 6. Hu B, Guo H, Zhou P, Shi ZL. Characteristics of SARS-CoV-2 and COVID-19. Nat  
706 Rev Microbiol. 2021;19(3):141-54. Epub 20201006. doi: 10.1038/s41579-020-00459-7. PubMed  
707 PMID: 33024307; PubMed Central PMCID: PMC7537588.
- 708 7. Tregoning JS, Flight KE, Higham SL, Wang Z, Pierce BF. Progress of the COVID-  
709 19 vaccine effort: viruses, vaccines and variants versus efficacy, effectiveness and escape. Nat  
710 Rev Immunol. 2021;21(10):626-36. Epub 20210809. doi: 10.1038/s41577-021-00592-1.



- 711 PubMed PMID: 34373623; PubMed Central PMCID: PMC8351583.
- 712 8. Pritchard E, Matthews PC, Stoesser N, Eyre DW, Gethings O, Vihta KD, et al.
- 713 Impact of vaccination on new SARS-CoV-2 infections in the United Kingdom. *Nat Med.*
- 714 2021;27(8):1370-8. Epub 20210609. doi: 10.1038/s41591-021-01410-w. PubMed PMID:
- 715 34108716; PubMed Central PMCID: PMC8363500.
- 716 9. Planas D, Veyer D, Baidaliuk A, Staropoli I, Guivel-Benhassine F, Rajah MM, et al.
- 717 Reduced sensitivity of SARS-CoV-2 variant Delta to antibody neutralization. *Nature.*
- 718 2021;596(7871):276-80. Epub 20210708. doi: 10.1038/s41586-021-03777-9. PubMed PMID:
- 719 34237773.
- 720 10. Tao K, Tzou PL, Nouhin J, Gupta RK, de Oliveira T, Kosakovsky Pond SL, et al. The
- 721 biological and clinical significance of emerging SARS-CoV-2 variants. *Nat Rev Genet.* 2021.
- 722 Epub 20210917. doi: 10.1038/s41576-021-00408-x. PubMed PMID: 34535792; PubMed
- 723 Central PMCID: PMC8447121.
- 724 11. Uriu K, Kimura I, Shirakawa K, Takaori-Kondo A, Nakada TA, Kaneda A, et al.
- 725 Neutralization of the SARS-CoV-2 Mu Variant by Convalescent and Vaccine Serum. *N Engl*
- 726 *J Med.* 2021. Epub 20211103. doi: 10.1056/NEJMc2114706. PubMed PMID: 34731554.
- 727 12. Mei M, Tan X. Current Strategies of Antiviral Drug Discovery for COVID-19. *Front*
- 728 *Mol Biosci.* 2021;8:671263. Epub 20210513. doi: 10.3389/fmolb.2021.671263. PubMed PMID:

- 729 34055887; PubMed Central PMCID: PMCPMC8155633.
- 730 13. Rando HM, Wellhausen N, Ghosh S, Lee AJ, Dattoli AA, Hu F, et al. Identification  
731 and Development of Therapeutics for COVID-19. *mSystems*. 2021:e0023321. Epub 20211102.  
732 doi: 10.1128/mSystems.00233-21. PubMed PMID: 34726496; PubMed Central PMCID:  
733 PMCPMC8562484.
- 734 14. Jackson CB, Farzan M, Chen B, Choe H. Mechanisms of SARS-CoV-2 entry into  
735 cells. *Nat Rev Mol Cell Biol*. 2021. Epub 20211005. doi: 10.1038/s41580-021-00418-x. PubMed  
736 PMID: 34611326; PubMed Central PMCID: PMCPMC8491763.
- 737 15. Hoffmann M, Kleine-Weber H, Pöhlmann S. A Multibasic Cleavage Site in the Spike  
738 Protein of SARS-CoV-2 Is Essential for Infection of Human Lung Cells. *Mol Cell*.  
739 2020;78(4):779-84.e5. Epub 20200501. doi: 10.1016/j.molcel.2020.04.022. PubMed PMID:  
740 32362314; PubMed Central PMCID: PMCPMC7194065.
- 741 16. Shang J, Wan Y, Luo C, Ye G, Geng Q, Auerbach A, et al. Cell entry mechanisms of  
742 SARS-CoV-2. *Proc Natl Acad Sci U S A*. 2020;117(21):11727-34. Epub 2020/05/06. doi:  
743 10.1073/pnas.2003138117. PubMed PMID: 32376634.
- 744 17. Yan R, Zhang Y, Li Y, Xia L, Guo Y, Zhou Q. Structural basis for the recognition of  
745 SARS-CoV-2 by full-length human ACE2. *Science*. 2020;367(6485):1444-8. Epub 20200304.  
746 doi: 10.1126/science.abb2762. PubMed PMID: 32132184; PubMed Central PMCID:

- 747 PMCPMC7164635.
- 748 18. Lan J, Ge J, Yu J, Shan S, Zhou H, Fan S, et al. Structure of the SARS-CoV-2 spike  
749 receptor-binding domain bound to the ACE2 receptor. *Nature*. 2020;581(7807):215-20. Epub  
750 20200330. doi: 10.1038/s41586-020-2180-5. PubMed PMID: 32225176.
- 751 19. Hoffmann M, Kleine-Weber H, Schroeder S, Krüger N, Herrler T, Erichsen S, et al.  
752 SARS-CoV-2 Cell Entry Depends on ACE2 and TMPRSS2 and Is Blocked by a Clinically  
753 Proven Protease Inhibitor. *Cell*. 2020;181(2):271-80.e8. Epub 2020/03/05. doi:  
754 10.1016/j.cell.2020.02.052. PubMed PMID: 32142651; PubMed Central PMCID:  
755 PMCPMC7102627.
- 756 20. Zhao MM, Yang WL, Yang FY, Zhang L, Huang WJ, Hou W, et al. Cathepsin L plays  
757 a key role in SARS-CoV-2 infection in humans and humanized mice and is a promising target  
758 for new drug development. *Signal Transduct Target Ther*. 2021;6(1):134. Epub 20210327. doi:  
759 10.1038/s41392-021-00558-8. PubMed PMID: 33774649; PubMed Central PMCID:  
760 PMCPMC7997800.
- 761 21. Murgolo N, Therien AG, Howell B, Klein D, Koeplinger K, Lieberman LA, et al.  
762 SARS-CoV-2 tropism, entry, replication, and propagation: Considerations for drug discovery  
763 and development. *PLoS Pathog*. 2021;17(2):e1009225. Epub 2021/02/17. doi:  
764 10.1371/journal.ppat.1009225. PubMed PMID: 33596266; PubMed Central PMCID:

- 765 PMCPMC7888651.
- 766 22. Koch J, Uckeley ZM, Doldan P, Stanifer M, Boulant S, Lozach PY. TMPRSS2  
767 expression dictates the entry route used by SARS-CoV-2 to infect host cells. *EMBO J*.  
768 2021;40(16):e107821. Epub 20210713. doi: 10.15252/emboj.2021107821. PubMed PMID:  
769 34159616; PubMed Central PMCID: PMCPMC8365257.
- 770 23. Bestle D, Heindl MR, Limburg H, Van Lam van T, Pilgram O, Moulton H, et al.  
771 TMPRSS2 and furin are both essential for proteolytic activation of SARS-CoV-2 in human  
772 airway cells. *Life Sci Alliance*. 2020;3(9). Epub 20200723. doi: 10.26508/lsa.202000786.  
773 PubMed PMID: 32703818; PubMed Central PMCID: PMCPMC7383062.
- 774 24. Yamamoto M, Kiso M, Sakai-Tagawa Y, Iwatsuki-Horimoto K, Imai M, Takeda M,  
775 et al. The Anticoagulant Nafamostat Potently Inhibits SARS-CoV-2 S Protein-Mediated  
776 Fusion in a Cell Fusion Assay System and Viral Infection In Vitro in a Cell-Type-Dependent  
777 Manner. *Viruses*. 2020;12(6). Epub 2020/06/10. doi: 10.3390/v12060629. PubMed PMID:  
778 32532094.
- 779 25. Yamamoto M, Matsuyama S, Li X, Takeda M, Kawaguchi Y, Inoue JI, et al.  
780 Identification of Nafamostat as a Potent Inhibitor of Middle East Respiratory Syndrome  
781 Coronavirus S Protein-Mediated Membrane Fusion Using the Split-Protein-Based Cell-Cell  
782 Fusion Assay. *Antimicrob Agents Chemother*. 2016;60(11):6532-9. Epub 2016/08/24. doi:

783 10.1128/aac.01043-16. PubMed PMID: 27550352; PubMed Central PMCID:  
784 PMC5075056.

785 26. Ishikawa H, Meng F, Kondo N, Iwamoto A, Matsuda Z. Generation of a dual-  
786 functional split-reporter protein for monitoring membrane fusion using self-associating split  
787 GFP. *Protein Eng Des Sel.* 2012;25(12):813-20. doi: 10.1093/protein/gzs051. PubMed PMID:  
788 22942393.

789 27. Wojtowicz-Praga S, Torri J, Johnson M, Steen V, Marshall J, Ness E, et al. Phase I  
790 trial of Marimastat, a novel matrix metalloproteinase inhibitor, administered orally to  
791 patients with advanced lung cancer. *J Clin Oncol.* 1998;16(6):2150-6. doi:  
792 10.1200/JCO.1998.16.6.2150. PubMed PMID: 9626215.

793 28. Hande KR, Collier M, Paradiso L, Stuart-Smith J, Dixon M, Clendeninn N, et al.  
794 Phase I and pharmacokinetic study of prinomastat, a matrix metalloprotease inhibitor. *Clin*  
795 *Cancer Res.* 2004;10(3):909-15. doi: 10.1158/1078-0432.ccr-0981-3. PubMed PMID: 14871966.

796 29. Standard of Care (SOC) With or Without CTS-1027 in Hepatitis C (HCV) Null-  
797 Responders <https://clinicaltrials.gov/ct2/show/results/NCT01273064>.

798 30. Vandenbroucke RE, Dejonckheere E, Libert C. A therapeutic role for matrix  
799 metalloproteinase inhibitors in lung diseases? *Eur Respir J.* 2011;38(5):1200-14. Epub  
800 20110609. doi: 10.1183/09031936.00027411. PubMed PMID: 21659416.

- 801 31. Jacobsen JA, Major Jourden JL, Miller MT, Cohen SM. To bind zinc or not to bind  
802 zinc: an examination of innovative approaches to improved metalloproteinase inhibition.  
803 *Biochim Biophys Acta.* 2010;1803(1):72-94. Epub 20090825. doi:  
804 10.1016/j.bbamcr.2009.08.006. PubMed PMID: 19712708.
- 805 32. Madoux F, Dreytmuller D, Pettiloud JP, Santos R, Becker-Pauly C, Ludwig A, et al.  
806 Discovery of an enzyme and substrate selective inhibitor of ADAM10 using an exosite-  
807 binding glycosylated substrate. *Sci Rep.* 2016;6(1):11. Epub 20161205. doi: 10.1038/s41598-  
808 016-0013-4. PubMed PMID: 28442704; PubMed Central PMCID: PMC5431342.
- 809 33. Liechti FD, Bächtold F, Grandgirard D, Leppert D, Leib SL. The matrix  
810 metalloproteinase inhibitor RS-130830 attenuates brain injury in experimental  
811 pneumococcal meningitis. *J Neuroinflammation.* 2015;12:43. Epub 20150304. doi:  
812 10.1186/s12974-015-0257-0. PubMed PMID: 25890041; PubMed Central PMCID:  
813 PMC4352253.
- 814 34. Hundhausen C, Misztela D, Berkhout TA, Broadway N, Saftig P, Reiss K, et al. The  
815 disintegrin-like metalloproteinase ADAM10 is involved in constitutive cleavage of CX3CL1  
816 (fractalkine) and regulates CX3CL1-mediated cell-cell adhesion. *Blood.* 2003;102(4):1186-95.  
817 Epub 20030424. doi: 10.1182/blood-2002-12-3775. PubMed PMID: 12714508.
- 818 35. Ludwig A, Hundhausen C, Lambert MH, Broadway N, Andrews RC, Bickett DM, et

819 al. Metalloproteinase inhibitors for the disintegrin-like metalloproteinases ADAM10 and  
820 ADAM17 that differentially block constitutive and phorbol ester-inducible shedding of cell  
821 surface molecules. *Comb Chem High Throughput Screen.* 2005;8(2):161-71. doi:  
822 10.2174/1386207053258488. PubMed PMID: 15777180.

823 36. Black RA, Rauch CT, Kozlosky CJ, Peschon JJ, Slack JL, Wolfson MF, et al. A  
824 metalloproteinase disintegrin that releases tumour-necrosis factor- $\alpha$  from cells. *Nature.*  
825 1997;385(6618):729-33. doi: 10.1038/385729a0. PubMed PMID: 9034190.

826 37. Schlomann U, Koller G, Conrad C, Ferdous T, Golfi P, Garcia AM, et al. ADAM8 as  
827 a drug target in pancreatic cancer. *Nat Commun.* 2015;6:6175. Epub 20150128. doi:  
828 10.1038/ncomms7175. PubMed PMID: 25629724; PubMed Central PMCID:  
829 PMC5014123.

830 38. Tamura Y, Watanabe F, Nakatani T, Yasui K, Fuji M, Komurasaki T, et al. Highly  
831 selective and orally active inhibitors of type IV collagenase (MMP-9 and MMP-2): N-  
832 sulfonylamino acid derivatives. *J Med Chem.* 1998;41(4):640-9. doi: 10.1021/jm9707582.  
833 PubMed PMID: 9484512.

834 39. Fray MJ, Dickinson RP, Huggins JP, Occleston NL. A potent, selective inhibitor of  
835 matrix metalloproteinase-3 for the topical treatment of chronic dermal ulcers. *J Med Chem.*  
836 2003;46(16):3514-25. doi: 10.1021/jm0308038. PubMed PMID: 12877590.

- 837 40. Levin JI, Chen J, Du M, Hogan M, Kincaid S, Nelson FC, et al. The discovery of  
838 anthranilic acid-based MMP inhibitors. Part 2: SAR of the 5-position and P1(1) groups.  
839 Bioorg Med Chem Lett. 2001;11(16):2189-92. doi: 10.1016/s0960-894x(01)00419-x. PubMed  
840 PMID: 11514167.
- 841 41. Dales NA, Gould AE, Brown JA, Calderwood EF, Guan B, Minor CA, et al.  
842 Substrate-based design of the first class of angiotensin-converting enzyme-related  
843 carboxypeptidase (ACE2) inhibitors. J Am Chem Soc. 2002;124(40):11852-3. doi:  
844 10.1021/ja0277226. PubMed PMID: 12358520.
- 845 42. Yeung ML, Teng JLL, Jia L, Zhang C, Huang C, Cai JP, et al. Soluble ACE2-  
846 mediated cell entry of SARS-CoV-2 via interaction with proteins related to the renin-  
847 angiotensin system. Cell. 2021;184(8):2212-28.e12. Epub 20210302. doi:  
848 10.1016/j.cell.2021.02.053. PubMed PMID: 33713620; PubMed Central PMCID:  
849 PMCPMC7923941.
- 850 43. Rodríguez E, Everitt E. Adenovirus uncoating and nuclear establishment are not  
851 affected by weak base amines. J Virol. 1996;70(6):3470-7. doi: 10.1128/JVI.70.6.3470-  
852 3477.1996. PubMed PMID: 8648679; PubMed Central PMCID: PMCPMC190220.
- 853 44. Zhang Z, Zheng Y, Niu Z, Zhang B, Wang C, Yao X, et al. SARS-CoV-2 spike protein  
854 dictates syncytium-mediated lymphocyte elimination. Cell Death Differ. 2021;28(9):2765-77.



- 855 Epub 20210420. doi: 10.1038/s41418-021-00782-3. PubMed PMID: 33879858; PubMed  
856 Central PMCID: PMCPMC8056997.
- 857 45. Bussani R, Schneider E, Zentilin L, Collesi C, Ali H, Braga L, et al. Persistence of  
858 viral RNA, pneumocyte syncytia and thrombosis are hallmarks of advanced COVID-19  
859 pathology. *EBioMedicine*. 2020;61:103104. Epub 20201103. doi: 10.1016/j.ebiom.2020.103104.  
860 PubMed PMID: 33158808; PubMed Central PMCID: PMCPMC7677597.
- 861 46. Hoffmann M, Schroeder S, Kleine-Weber H, Müller MA, Drosten C, Pöhlmann S.  
862 Nafamostat mesylate blocks activation of SARS-CoV-2: New treatment option for COVID-19.  
863 *Antimicrob Agents Chemother*. 2020. Epub 2020/04/20. doi: 10.1128/AAC.00754-20. PubMed  
864 PMID: 32312781.
- 865 47. Fan C, Lu W, Li K, Ding Y, Wang J. ACE2 Expression in Kidney and Testis May  
866 Cause Kidney and Testis Infection in COVID-19 Patients. *Front Med (Lausanne)*.  
867 2020;7:563893. Epub 20210113. doi: 10.3389/fmed.2020.563893. PubMed PMID: 33521006;  
868 PubMed Central PMCID: PMCPMC7838217.
- 869 48. Liu J, Li Y, Liu Q, Yao Q, Wang X, Zhang H, et al. SARS-CoV-2 cell tropism and  
870 multiorgan infection. *Cell Discov*. 2021;7(1):17. Epub 20210323. doi: 10.1038/s41421-021-  
871 00249-2. PubMed PMID: 33758165; PubMed Central PMCID: PMCPMC7987126.
- 872 49. Reis FM, Bouissou DR, Pereira VM, Camargos AF, dos Reis AM, Santos RA.

- 873 Angiotensin-(1-7), its receptor Mas, and the angiotensin-converting enzyme type 2 are  
874 expressed in the human ovary. *Fertil Steril.* 2011;95(1):176-81. Epub 20100801. doi:  
875 10.1016/j.fertnstert.2010.06.060. PubMed PMID: 20674894.
- 876 50. Jing Y, Run-Qian L, Hao-Ran W, Hao-Ran C, Ya-Bin L, Yang G, et al. Potential  
877 influence of COVID-19/ACE2 on the female reproductive system. *Mol Hum Reprod.*  
878 2020;26(6):367-73. doi: 10.1093/molehr/gaaa030. PubMed PMID: 32365180; PubMed Central  
879 PMCID: PMCPMC7239105.
- 880 51. Henarejos-Castillo I, Sebastian-Leon P, Devesa-Peiro A, Pellicer A, Diaz-Gimeno P.  
881 SARS-CoV-2 infection risk assessment in the endometrium: viral infection-related gene  
882 expression across the menstrual cycle. *Fertil Steril.* 2020;114(2):223-32. Epub 20200617. doi:  
883 10.1016/j.fertnstert.2020.06.026. PubMed PMID: 32641214; PubMed Central PMCID:  
884 PMCPMC7298504.
- 885 52. Puelles VG, Lütgehetmann M, Lindenmeyer MT, Sperhake JP, Wong MN, Allweiss  
886 L, et al. Multiorgan and Renal Tropism of SARS-CoV-2. *N Engl J Med.* 2020;383(6):590-2.  
887 Epub 2020/05/13. doi: 10.1056/NEJMc2011400. PubMed PMID: 32402155; PubMed Central  
888 PMCID: PMCPMC7240771.
- 889 53. Diao B, Wang C, Wang R, Feng Z, Zhang J, Yang H, et al. Human kidney is a target  
890 for novel severe acute respiratory syndrome coronavirus 2 infection. *Nat Commun.*

891 2021;12(1):2506. Epub 20210504. doi: 10.1038/s41467-021-22781-1. PubMed PMID:  
892 33947851; PubMed Central PMCID: PMC8096808.

893 54. Johnson BA, Xie X, Bailey AL, Kalveram B, Lokugamage KG, Muruato A, et al. Loss  
894 of furin cleavage site attenuates SARS-CoV-2 pathogenesis. *Nature*. 2021;591(7849):293-9.  
895 Epub 20210125. doi: 10.1038/s41586-021-03237-4. PubMed PMID: 33494095; PubMed  
896 Central PMCID: PMC8175039.

897 55. Peacock TP, Goldhill DH, Zhou J, Baillon L, Frise R, Swann OC, et al. The furin  
898 cleavage site in the SARS-CoV-2 spike protein is required for transmission in ferrets. *Nat*  
899 *Microbiol*. 2021;6(7):899-909. Epub 20210427. doi: 10.1038/s41564-021-00908-w. PubMed  
900 PMID: 33907312.

901 56. Benton DJ, Wrobel AG, Xu P, Roustan C, Martin SR, Rosenthal PB, et al. Receptor  
902 binding and priming of the spike protein of SARS-CoV-2 for membrane fusion. *Nature*.  
903 2020;588(7837):327-30. Epub 20200917. doi: 10.1038/s41586-020-2772-0. PubMed PMID:  
904 32942285; PubMed Central PMCID: PMC8116727.

905 57. Stevens CS, Oguntuyo KY, Lee B. Proteases and variants: context matters for  
906 SARS-CoV-2 entry assays. *Curr Opin Virol*. 2021;50:49-58. Epub 20210724. doi:  
907 10.1016/j.coviro.2021.07.004. PubMed PMID: 34365113; PubMed Central PMCID:  
908 PMC8302850.

- 909 58. Harvey WT, Carabelli AM, Jackson B, Gupta RK, Thomson EC, Harrison EM, et al.  
910 SARS-CoV-2 variants, spike mutations and immune escape. *Nat Rev Microbiol.*  
911 2021;19(7):409-24. Epub 20210601. doi: 10.1038/s41579-021-00573-0. PubMed PMID:  
912 34075212; PubMed Central PMCID: PMCPMC8167834.
- 913 59. The human protein atlas - Tissue expression of  
914 ADAM10 <https://www.proteinatlas.org/ENSG00000137845-ADAM10/tissue>.
- 915 60. The human protein atlas - Cell type atlas  
916 <https://www.proteinatlas.org/ENSG00000137845-ADAM10/celltype>.
- 917 61. Caescu CI, Jeschke GR, Turk BE. Active-site determinants of substrate recognition  
918 by the metalloproteinases TACE and ADAM10. *Biochem J.* 2009;424(1):79-88. Epub  
919 20091023. doi: 10.1042/BJ20090549. PubMed PMID: 19715556; PubMed Central PMCID:  
920 PMCPMC2774824.
- 921 62. Carapito R, Li R, Helms J, Carapito C, Gujja S, Rolli V, et al. Identification of driver  
922 genes for critical forms of COVID-19 in a deeply phenotyped young patient cohort. *Sci Transl*  
923 *Med.* 2021:eabj7521. Epub 20211026. doi: 10.1126/scitranslmed.abj7521. PubMed PMID:  
924 34698500.
- 925 63. Daniloski Z, Jordan TX, Wessels HH, Hoagland DA, Kasela S, Legut M, et al.  
926 Identification of Required Host Factors for SARS-CoV-2 Infection in Human Cells. *Cell.*

- 927 2021;184(1):92-105.e16. Epub 20201024. doi: 10.1016/j.cell.2020.10.030. PubMed PMID:  
928 33147445; PubMed Central PMCID: PMC7584921.
- 929 64. Gunst JD, Staerke NB, Pahus MH, Kristensen LH, Bodilsen J, Lohse N, et al.  
930 Efficacy of the TMPRSS2 inhibitor camostat mesilate in patients hospitalized with Covid-19-  
931 a double-blind randomized controlled trial. *EClinicalMedicine*. 2021;35:100849. Epub  
932 20210422. doi: 10.1016/j.eclinm.2021.100849. PubMed PMID: 33903855; PubMed Central  
933 PMCID: PMC8060682.
- 934 65. Boulware DR, Pullen MF, Bangdiwala AS, Pastick KA, Lofgren SM, Okafor EC, et  
935 al. A Randomized Trial of Hydroxychloroquine as Postexposure Prophylaxis for Covid-19. *N*  
936 *Engl J Med*. 2020;383(6):517-25. Epub 20200603. doi: 10.1056/NEJMoa2016638. PubMed  
937 PMID: 32492293; PubMed Central PMCID: PMC7289276.
- 938 66. Self WH, Semler MW, Leither LM, Casey JD, Angus DC, Brower RG, et al. Effect of  
939 Hydroxychloroquine on Clinical Status at 14 Days in Hospitalized Patients With COVID-19:  
940 A Randomized Clinical Trial. *JAMA*. 2020;324(21):2165-76. doi: 10.1001/jama.2020.22240.  
941 PubMed PMID: 33165621; PubMed Central PMCID: PMC7653542.
- 942 67. Matsuyama S, Nao N, Shirato K, Kawase M, Saito S, Takayama I, et al. Enhanced  
943 isolation of SARS-CoV-2 by TMPRSS2-expressing cells. *Proc Natl Acad Sci U S A*.  
944 2020;117(13):7001-3. Epub 2020/03/12. doi: 10.1073/pnas.2002589117. PubMed PMID:

- 945 32165541; PubMed Central PMCID: PMCPMC7132130.
- 946 68. Wang H, Li X, Nakane S, Liu S, Ishikawa H, Iwamoto A, et al. Co-expression of  
947 foreign proteins tethered to HIV-1 envelope glycoprotein on the cell surface by introducing  
948 an intervening second membrane-spanning domain. PLoS One. 2014;9(5):e96790. doi:  
949 10.1371/journal.pone.0096790. PubMed PMID: 24804933; PubMed Central PMCID:  
950 PMCPMC4013048.
- 951 69. Imai M, Iwatsuki-Horimoto K, Hatta M, Loeber S, Halfmann PJ, Nakajima N, et al.  
952 Syrian hamsters as a small animal model for SARS-CoV-2 infection and countermeasure  
953 development. Proc Natl Acad Sci U S A. 2020;117(28):16587-95. Epub 20200622. doi:  
954 10.1073/pnas.2009799117. PubMed PMID: 32571934; PubMed Central PMCID:  
955 PMCPMC7368255.
- 956 70. Yamamoto M, Abe C, Wakinaga S, Sakane K, Yumiketa Y, Taguchi Y, et al. TRAF6  
957 maintains mammary stem cells and promotes pregnancy-induced mammary epithelial cell  
958 expansion. Commun Biol. 2019;2:292. Epub 2019/08/06. doi: 10.1038/s42003-019-0547-7.  
959 PubMed PMID: 31396572; PubMed Central PMCID: PMCPMC6684589.
- 960 71. Tani H, Shiokawa M, Kaname Y, Kambara H, Mori Y, Abe T, et al. Involvement of  
961 ceramide in the propagation of Japanese encephalitis virus. J Virol. 2010;84(6):2798-807.  
962 Epub 20100106. doi: 10.1128/JVI.02499-09. PubMed PMID: 20053738; PubMed Central

963 PMID: PMCPMC2826033.

964

965 **Additional information**

966 **Financial Disclosure Statement**

967 This work was supported, in part, by the Platform Project for Supporting Drug Discovery  
968 and Life Science Research from the Japan Agency for Medical Research and  
969 Development (AMED) under Grant Number JP20am0101086 (support number 2834),  
970 and by grants-in-aid from the Ministry of Education, Culture, Sports, Science, and  
971 Technology, Japan (MEXT; 16H06575 to JI), from the Japanese Society for the  
972 Promotion of Science (JSPS; 15K21438 and 18K15235 to MY), from AMED [Program  
973 of Japan Initiative for Global Research Network on Infectious Diseases (JGRID)  
974 JP20wm0125002 to YK], and from the University of Tokyo (Promoting practical use of  
975 measures against coronavirus disease 2019 [COVID-19] to JI). The funders had no role  
976 in study design, data collection and analysis, decision to publish, or preparation of the  
977 manuscript.

978

979 **Competing interests:** The authors declare no competing interests.

980

981 **Figure Captions**

982 **Fig 1. ACE2-dependent but TMPRSS2-independent membrane fusion activity of the**  
983 **SARS-CoV-2 S protein**

984 (a) Cell fusion kinetics induced by the S proteins from SARS-CoV, SARS-CoV-2, and  
985 MERS-CoV were determined using the DSP assay. Target cells expressing ACE2 alone  
986 or together with TMPRSS2 were used for co-culturing with effector cells expressing  
987 SARS-CoV S and SARS-CoV-2 S, and cells expressing CD26 alone or together with  
988 TMPRSS2 were used for co-culturing with effector cells expressing MERS-CoV- S.  
989 Relative cell-fusion values were calculated by normalizing the RL activity of each co-  
990 culture to that of the co-culture with cells expressing both receptor and TMPRSS2 at 240  
991 min, which was set to 100%. Values are means  $\pm$  SD ( $n = 3$ /group). \*\*  $p < 0.01$ . (b) Phase  
992 contrast images of S protein-mediated cell fusion 16 h after co-culture. Red arrowheads  
993 indicate syncytia formation Scale bars, 100  $\mu$ m. (c) Effect of nafamostat on the  
994 TMPRSS2-dependent cell fusion. Target cells expressing ACE2 with TMPRSS2 were  
995 used for co-culturing with effector cells expressing SARS-CoV S and SARS-CoV-2 S,  
996 and cells expressing CD26 with TMPRSS2 were used for co-culturing with effector cells  
997 expressing MERS-CoV- S. Relative cell-fusion values were calculated by normalizing  
998 the RL activity for each co-culture to that of the co-culture with cells expressing both



999 receptor and TMPRSS2 in the presence of DMSO, which was set to 100%. Values are  
1000 means  $\pm$  SD ( $n = 3/\text{group}$ ). \*\*  $p < 0.01$ . **(d)** Effects of the nafamostat on the TMPRSS2-  
1001 independent or -dependent cell fusion. Target cells expressing ACE2 alone or together  
1002 with TMPRSS2 were used for co-culturing with effector cells expressing SARS-CoV-2  
1003 S. Relative cell-fusion value was calculated by normalizing the RL activity for each co-  
1004 culture to that of the co-culture with cells expressing both ACE2 and TMPRSS2 in the  
1005 presence of DMSO, which was set to 100%. Values are means  $\pm$  SD ( $n = 3/\text{group}$ ). nafamo,  
1006 nafamostat.

1007

1008 **Fig 2. TMPRSS2-independent membrane fusion induced by the S protein of SARS-**  
1009 **CoV-2 is blocked by various metalloproteinase inhibitors.**

1010 **(a)** High-throughput screening of the Validated Compound Library (1,630 clinically  
1011 approved compounds and 1,885 pharmacologically active compounds) in the DSP assay  
1012 using the SARS-CoV-2 S protein. The x-axis shows the relative cell-fusion value using  
1013 cells expressing both TMPRSS2 and ACE2 in the presence of each compound (1  $\mu\text{M}$  in  
1014 DMSO),  $n = 1$ . The y-axis shows the relative cell-fusion value using cells expressing  
1015 ACE2 alone in the presence of each compound (1  $\mu\text{M}$  in DMSO),  $n = 1$ . The relative cell-  
1016 fusion value was calculated by normalizing the RL activity for each compound to that of

1017 the control assay (DMSO alone; set to 100%). Each dot represents an individual  
1018 compound. Dots in the red-dashed box indicate compounds that preferentially inhibit  
1019 TMPRSS2-independent membrane fusion. (< 30% inhibition of the relative cell fusion  
1020 value using the target cells expressing both TMPRSS2 and ACE2 and > 40% inhibition  
1021 of the relative cell-fusion value using the target cells expressing ACE2 alone. The  
1022 compound names for the candidates are indicated. (b) Effects of the metalloproteinase  
1023 inhibitors on cell fusion in the co-cultures of the cells expressing SARS-CoV-2 S protein  
1024 with those expressing ACE2 alone or in combination with TMPRSS2. Relative cell-  
1025 fusion values were calculated by normalizing the RL activity for each co-culture to that  
1026 of the co-culture with cells expressing both ACE2 and TMPRSS2 in the presence of  
1027 DMSO, which was set to 100%. Values are means  $\pm$  SD ( $n = 3$ /group). \*\*  $p < 0.01$ .

1028

1029 **Fig 3. The metalloproteinase-dependent viral entry pathway is cell type-dependent.**

1030 Effects of drugs on the entry of SARS-CoV-2 S-bearing vesicular stomatitis virus (VSV)  
1031 pseudotype virus. The relative pseudovirus entry was calculated by normalizing the FL  
1032 activity for each condition to the FL activity of cells infected with SARS-CoV-2 S-  
1033 bearing pseudovirus in the presence of DMSO alone, which was set to 100%. Values are  
1034 means  $\pm$  SD ( $n = 3$ /group). \*  $p < 0.05$ , \*\*  $p < 0.01$ . Cont: cells infected with pseudovirus

1035 without S protein; SARS-CoV-2: cells infected with SARS-CoV-2 S-bearing pseudovirus.  
1036 E-64d: 25  $\mu$ M E-64d, nafamo: 10  $\mu$ M nafamostat, marima: 1  $\mu$ M marimastat. **(a)** Effects  
1037 of marimastat, E-64d, or nafamostat on the pseudovirus entry in A704, OVISe, and Calu-  
1038 3 cells, respectively. **(b-e)** Effects of a single drug treatment or a combination treatment  
1039 on the pseudovirus entry in VeroE6, HEC50B, OVTOKO and A704 cells (b), IGROV1,  
1040 OUMS-23 and OVISe cells (c), Calu-3 and Caco-2 (d), and HEC50B-TMPRSS2 cells  
1041 (e).

1042

1043 **Fig 4. The metalloproteinase-dependent entry pathway requires both the furin-**  
1044 **cleavage site and S2 region of the SARS-CoV-2 S protein.**

1045 Effects of drugs on the entry of S protein-bearing vesicular stomatitis virus (VSV)  
1046 pseudotype virus. The relative pseudovirus entry was calculated by normalizing the FL  
1047 activity for each condition to the FL activity of cells infected with pseudovirus in the  
1048 presence of DMSO alone, which was set to 100%. Values are means  $\pm$  SD ( $n = 3$ /group).

1049 \*\*  $p < 0.01$ . Cont: cells infected with pseudovirus without S protein. E-64d: 25  $\mu$ M E-  
1050 64d, marima: 1  $\mu$ M marimastat, nafamo: 10  $\mu$ M nafamostat. **(a)** Effects of E-64d and  
1051 marimastat on the entry of pseudoviruses bearing SARS-CoV S, SARS-CoV-2 S, MERS-  
1052 CoV S, or VSV G in HEC50B cells. **b**, Effects of E-64d and marimastat on the entry of

1053 HCoV-NL63 S and WIV1-CoV S pseudovirus in HEC50B cells. **c**, Schematic illustration  
1054 of C-terminally Flag-tagged chimeric S proteins in which the S1, S1/S2 boundary, and  
1055 S2 domain from SARS-CoV S (red) or SARS-CoV-2 S (yellow) are indicated (top).  
1056 Amino acid sequences of the residues around the S1/S2 boundary of the coronaviruses  
1057 (bottom). Numbers refer to the amino acid residues. F: Flag-tag. Arginine residues in the  
1058 S1/S2 cleavage site and furin cleavage motif are highlighted in red. **(d)** Expression of  
1059 chimeric S protein in pseudoviruses. S proteins were detected using an anti-Flag-tag  
1060 antibody that binds to a Flag-tag on the C-terminus of the S proteins (top). Detection of  
1061 the vesicular stomatitis virus matrix protein (VSV M) served as the control (bottom). S0:  
1062 uncleaved S protein; S2: cleaved S2 domain of the S protein. **(e, f)** Effects of E-64d and  
1063 marimastat on the entry of pseudoviruses bearing chimeric S proteins in HEC50B cells.  
1064 **(g)** Effects of E-64d and nafamostat on the entry of pseudoviruses bearing SARS-CoV S,  
1065 SARS-CoV-2 S, MERS-CoV S, or VSV G in HEC50B-TMPRSS2 cells in the presence  
1066 of marimastat. **(h, i)** Effects of E-64d and nafamostat on the entry of pseudoviruses  
1067 bearing chimeric S proteins in HEC50B-TMPRSS2 cells in the presence of marimastat.  
1068  
1069 **Fig 5. Possible involvement of ADAM-10 in the metalloproteinase-dependent entry**  
1070 **of SARS-CoV-2.**

1071 (a) Effects of metalloprotease inhibitors on the entry of pseudoviruses bearing SARS-  
1072 CoV-2 S or VSV G in VeroE6 and HEC50B cells in the presence of E-64d, and A704  
1073 cells in the absence of E-64d. The relative pseudovirus entry was calculated by  
1074 normalizing the FL activity for each condition to the FL activity of cells infected with  
1075 pseudovirus in the presence of DMSO alone, which was set to 100%. Values are means  
1076  $\pm$  SD ( $n = 3$ /group). Data were compared with those obtained from cells infected  
1077 pseudoviruses bearing SARS-CoV-2 S in the presence of E-64d for HEC50B and VeroE6,  
1078 and in the presence of DMSO alone for A704. \*  $p < 0.05$ , \*\*  $p < 0.01$ . Cont: cells infected  
1079 with pseudovirus without S protein. marima: marimastat, prinoma: prinomastat, iloma:  
1080 ilomastat, CTS: CTS-1027, UK: UK370106, GW: GW280264X, GI: GI254023X, MLN:  
1081 MLN-4760, BK: BK-1361, MMP2/9i: MMP2/9 inhibitor I, MMP9i: MMP9 inhibitor I.  
1082 (b) Effects of the ADAM10 knockdown on ACE2 (top), ADAM10 (middle), and tubulin  
1083 (bottom) expression. HEC50B cells were transfected with two distinct control siRNAs or  
1084 three distinct siRNAs against Adam10 for 48 h. (c) The effect of the ADAM10  
1085 knockdown on the entry of pseudoviruses bearing SARS-CoV-2 S, SARS-CoV S,  
1086 MERS-CoV S, or VSV G. HEC50B cells were transfected with siRNAs for 48 h and then  
1087 infected with pseudoviruses. The relative pseudovirus entry was calculated by  
1088 normalizing the FL activity for each condition to the FL activity of cells infected with

1089 pseudovirus in the absence of siRNA (mock), which was set to 100%. Values are means  
1090  $\pm$  SD ( $n = 3$ /group). \*  $p < 0.05$ , \*\*  $p < 0.01$ . **(d, e)** Effect of ADAM10 knockdown on the  
1091 patterns of the entry pathways for SARS-CoV-2 S pseudovirus in HEC50B cells.  
1092 HEC50B cells were transfected with siRNAs for 48 h and then infected with  
1093 pseudoviruses in the presence of drugs. Values are means  $\pm$  SD ( $n = 3$ /group). \*\*  $p < 0.01$ .  
1094 E-64d: 25  $\mu$ M E-64d, marima: 1  $\mu$ M marimastat. Data are displayed as the conditions of  
1095 siRNA treatment (d) and drug treatment (e).

1096

1097 **Fig 6. The metalloproteinase-dependent entry pathway of authentic SARS-CoV-2 is**  
1098 **involved in syncytia formation and cytopathicity.**

1099 Effects of the drugs on the cytoplasmic viral RNA after SARS-CoV-2 infection. The  
1100 relative amount of viral RNA in the cells was normalized to cellular *Rpl13a* mRNA  
1101 expression. Values are means  $\pm$  SD ( $n = 3$ /group in a-d,  $n = 10$ /group in e). \*  $p < 0.05$ , \*\*  
1102  $p < 0.01$ . **(a)** Effects of marimastat or prinomastat on SARS-CoV-2 infection in HEC50B,  
1103 A704, and VeroE6 cells. **(b)** Effects of marimastat and the inhibitor of the endosome  
1104 pathway on SARS-CoV-2 infection in HEC50B, A704, and VeroE6 cells. marima: 1  $\mu$ M  
1105 marimastat, E-64d: 25  $\mu$ M E-64d, NH<sub>4</sub>Cl: 10 mM NH<sub>4</sub>Cl. **(c)** Effect of marimastat, E-  
1106 64d, and nafamostat on SARS-CoV-2 infection in HEC50B-TMPRSS2 cells. marima: 1

1107  $\mu$ M marimastat, E-64d: 25  $\mu$ M E-64d, nafamo: 10  $\mu$ M nafamostat. **(d)** Effects of selective  
1108 metalloprotease inhibitors on SARS-CoV-2 infection in HEC50B cells. GW:  
1109 GW280264X, GI: GI254023X. **(e)** Effect of ADAM10 knockdown on SARS-CoV-2  
1110 infection in HEC50B cells. **(f, g)** Effects of drugs on SARS-CoV-2-induced syncytia  
1111 formation in HEC50B (f) and HEC50B-TMPRSS2 (g) cells. Cells were stained with anti-  
1112 SARS-CoV-2 N antibody (green) 24 h after infection. Nuclei were stained with Hoechst  
1113 33342 (blue). Scale bars, 200  $\mu$ m. **(h, i)** Effects of drugs on SARS-CoV-2-induced  
1114 cytopathicity in HEC50B (h) and HEC50B-TMPRSS2 (i) cells. marima: marimastat,  
1115 prinoma: prinomastat. E-64d: 25  $\mu$ M E-64d, nafamo: 10  $\mu$ M nafamostat. Values are  
1116 means  $\pm$  SD ( $n = 3$ /group). \*\*  $p < 0.01$ .

1117

## 1118 **Supporting information**

1119 **S1 Fig. Cell-based membrane-fusion assay for coronavirus S proteins using the DSP**  
1120 **reporter.**

1121 **(a)** A method to monitor cell-cell membrane fusion mediated by the S protein of  
1122 coronaviruses[24, 25]. Effector cells (293FT cells expressing DSP8-11 and S protein) and  
1123 target cells (293FT cells expressing DSP1-7 and receptor protein with TMPRSS2 for “cell  
1124 fusion with TMPRSS2” (top) or receptor protein without TMPRSS2 for “cell fusion

1125 without TMPRSS2” (bottom)) were co-cultured for 4 h. Both GFP (fluorescence) and RL  
1126 (luminescence) signals were generated following DSP1-7 and DSP8-11 reassociation  
1127 upon mixing of the cells during the assay. **(b)** Expression of S proteins in effector cells  
1128 were detected using an anti-Flag-tag antibody that binds to a Flag-tag on the C-terminus  
1129 of S proteins (top). Tubulin was used as a control (bottom panel). S0: uncleaved S protein;  
1130 S2: cleaved S2 domain of the S protein. **(c)** Schematic diagram of split chimeric reporter  
1131 proteins. DSP1-7 has the structure RL1–155-Ser-Gly-Gly-Gly-Gly-GFP1–156. DSP8-11  
1132 has the Met- GFP157–231 -Gly-Gly-Gly-Gly-Ser- RL156–311. As GFP1–156 contains  
1133 the first seven  $\beta$  sheets, and GFP157–231 contains the remaining four  $\beta$  sheets, the split  
1134 proteins were called DSP1-7 and DSP8-11, respectively. DSP1-7 and DSP8-11  
1135 reassociate efficiently, resulting in the reconstitution of functional RL and GFP to  
1136 generate luminescent and fluorescent signals, respectively.

1137

1138 **S2 Fig. Control experiments for the DSP assay.**

1139 **(a)** A method to check whether compounds directly inhibit DSP activity without affecting  
1140 cell-cell fusion[25]. 293FT cells expressing DSP1-7 and DSP8-11 were treated with  
1141 compounds for 4 h. Measuring RL activities of the preformed DSP1-7/DSP8-11 complex  
1142 to check whether the compounds directly inhibit RL activities without affecting cell-cell



1143 fusion. **(b)** Effect of metalloproteinase inhibitors on RL activity. Relative DSP activity  
1144 was calculated by normalizing the RL activity for each condition to that of the control  
1145 assay (DMSO alone; set to 100%). Values are means  $\pm$  SD ( $n = 3$ /group).

1146

1147 **S3 Fig. Effects of candidate compounds on the cell-cell fusion and RL activities.**

1148 Effector cells expressing SARS-CoV-2 S were co-cultured with target cells expressing  
1149 ACE2 alone for the TMPRSS2-independent cell-cell fusion assay (blue) or cells  
1150 expressing ACE2 with TMPRSS2 for the TMPRSS2-dependent cell-cell fusion assay  
1151 (red) in the presence of candidate compounds for 4 h. Cells expressing DSP1-7 and DSP8-  
1152 11 in the presence of candidate compounds for 4 h to determine whether compounds  
1153 directly inhibit RL activities (purple). Relative DSP activity was calculated by  
1154 normalizing the RL activity for each condition to that of the control assay (DMSO alone;  
1155 set to 100%). Values are means  $\pm$  SD ( $n = 3$ /group).

1156

1157 **S4 Fig. The metalloproteinase-dependent entry pathway strictly requires both the**  
1158 **furin-cleavage site and S2 region of S protein of SARS-CoV-2.**

1159 Effects of the drugs on the entry of S protein-bearing vesicular stomatitis virus (VSV)  
1160 pseudotype virus. The relative pseudovirus entry was calculated by normalizing the FL

1161 activity for each condition to the FL activity of the cells infected with pseudovirus in the  
1162 presence of DMSO alone, which was set to 100%. Values are means  $\pm$  SD ( $n = 3$ /group).  
1163 \*\*  $p < 0.01$ . Cont: cells infected with pseudovirus without S protein. E-64d: 25  $\mu$ M E-  
1164 64d, marima: 1  $\mu$ M marimastat, nafamo: 10  $\mu$ M nafamostat. **(a, b)** Effects of E-64d and  
1165 marimastat on the entry of pseudoviruses bearing SARS-CoV S, SARS-CoV-2 S, MERS-  
1166 CoV S, or VSV G in A704 (a) and VeroE6 (b) cells. **(c, d)** Effects of E-64d and  
1167 marimastat on the entry of pseudoviruses bearing chimeric S proteins in VeroE6 cells. **(e)**  
1168 Effects of E-64d and nafamostat on the entry of pseudoviruses bearing SARS-CoV S,  
1169 SARS-CoV-2 S, MERS-CoV S, or VSV G in VeroE6-TMPRSS2 cells. **(f, g)** Effects of  
1170 E-64d and nafamostat on the entry of pseudoviruses bearing chimeric S proteins in  
1171 VeroE6-TMPRSS2 cells. To establish VeroE6 cells expressing TMPRSS2 (VeroE6-  
1172 TMPRSS2), recombinant pseudotype lentivirus expressing TMPRSS2 was produced  
1173 using 293T cells with a VSV-G-expressing plasmid. Cells infected with pseudotype  
1174 viruses were selected with 300  $\mu$ g/mL hygromycin for at least 1 week.

1175

1176 **S5 Fig. Patterns of entry pathways were conserved in various variants of SARS-**  
1177 **CoV-2.**

1178 (a) Expression of WT or mutant SARS-CoV-2 S proteins with mutations present in  
1179 B.1.1.7, B.1.351, B.1.617.1 and B.1.617.2 variants in the pseudoviruses. S proteins were  
1180 detected using an anti-Flag-tag antibody that binds to a Flag-tag on the C-terminus of S  
1181 proteins (top). Detection of vesicular stomatitis virus matrix protein (VSV M) served as  
1182 a control (bottom). S0: uncleaved S protein; S2: cleaved S2 domain of the S protein. (b)  
1183 Effects of E-64d and marimastat on the entry of pseudoviruses bearing SARS-CoV-2 S  
1184 in VeroE6 cells. E-64d: 25  $\mu$ M E-64d, marima: 1  $\mu$ M marimastat. (c) Effects of  
1185 nafamostat on the entry of pseudovirus bearing SARS-CoV-2 S in VeroE6-TMPRSS2  
1186 cells. (d) Effects of E-64d and marimastat on the entry of pseudoviruses bearing SARS-  
1187 CoV-2 S in HEC50B cells. E-64d: 25  $\mu$ M E-64d, marima: 1  $\mu$ M marimastat. (e) Effects  
1188 of marimastat on the entry of pseudoviruses bearing SARS-CoV-2 S in A704 cells. (f)  
1189 Effects of nafamostat on the entry of pseudoviruses bearing SARS-CoV-2 S in Calu-3  
1190 cells. The relative pseudovirus entry was calculated by normalizing the FL activity for  
1191 each condition to the FL activity of cells infected with pseudovirus in the presence of  
1192 DMSO alone, which was set to 100%. Values are means  $\pm$  SD ( $n = 3$ /group in b-f). Data  
1193 were compared with those obtained from cells infected pseudoviruses bearing variant  
1194 SARS-CoV-2 S in the presence of DMSO alone. \*  $p < 0.05$ , \*\*  $p < 0.01$ . Cont: cells  
1195 infected with a pseudovirus without S protein in (b-f).

1196

1197 **S6 Fig. Expression of WIV1-CoV and HCoV-NL63 S protein in pseudoviruses.**

1198 (a) Schematic illustration of C-terminally FLAG-tagged S proteins of WIV1-CoV and  
1199 HCoV-NL63 and amino acid sequences of the residues around the S1/S2 boundary of the  
1200 coronaviruses (bottom). Numbers refer to amino acid residues. F: Flag tag. Arginine  
1201 residues in the S1/S2 cleavage site and furin cleavage motif are highlighted in red. (b)  
1202 Expression of S protein in pseudoviruses S proteins were detected using an anti-Flag-tag  
1203 antibody that binds to a Flag-tag on the C-terminus of S proteins (top). The detection of  
1204 VSV M served as a control (bottom). S0: uncleaved S protein; S2: cleaved S2 domain of  
1205 the S protein.

1206

1207 **S7 Fig. Effects of drugs on cell viabilities.**

1208 (a-c) VeroE6 (a), HEC50B (b), and A704 (c) cells were treated with various drugs, and  
1209 cell viability was analyzed using Celltiter-Glo 24 h after the treatment. The relative cell  
1210 viability was calculated by normalizing the FL activity for each condition to the FL  
1211 activity of the cells in the presence of DMSO alone, which was set to 100%. Values are  
1212 means  $\pm$  SD ( $n = 3$ /group). (d, e) HEC50B (d), and HEC50B-TMPRSS2 (e) cells were  
1213 treated with various drugs for 3 days. Half of the culture supernatant was replaced daily

1214 with fresh medium containing the drugs. The relative cell viability was calculated by  
1215 normalizing the FL activity for each condition to the FL activity of cells in the presence  
1216 of DMSO alone, which was set to 100%. Values are means  $\pm$  SD ( $n = 6$ /group).

1217

1218 **S8 Fig. Patterns of the entry pathways of the pseudovirus bearing SARS-CoV-2 S**  
1219 **were not affected by the ADAM17 knockout in the HEC50B cells.**

1220 (a) Effect of the ADAM17 knockout on ACE2 (top), ADAM17 (middle), and tubulin

1221 (bottom). (b) Effect of the ADAM17 knockout on the entry of the pseudoviruses bearing

1222 SARS-CoV-2 S. Values are means  $\pm$  SD ( $n = 3$ /group). \*\*  $p < 0.01$ . (c) Effect of the

1223 ADAM17 knockout on the patterns of the entry pathways of SARS-CoV-2 S pseudovirus

1224 in HEC50B cells. The relative pseudovirus entry was calculated by normalizing the FL

1225 activity for each condition to the FL activity of cells infected with pseudovirus in the

1226 presence of DMSO alone, which was set to 100%. Values are means  $\pm$  SD ( $n = 3$ /group).

1227 \*  $p < 0.05$ , \*\*  $p < 0.01$ . E-64d: 25  $\mu$ M E-64d, marima: 1  $\mu$ M marimastat. To establish the

1228 ADAM17-knockout HEC50B cells, lentiviruses were produced by transfecting the

1229 lentiCRISPRv2 vector (#52961 Addgene, MA, USA) with the following gRNA

1230 sequences. The gRNA sequences used were 5'-GCG AGG TAT TCG GCT CCG CG-3'

1231 (Cont #1), 5'-GCT TTC ACG GAG GTT CGA CG-3' (Cont #2) and 5'-ATG TTG CAG

1232 TTC GGC TCG AT-3' (Cont #3) for the control experiments, and 5'-AAC GTT CAG  
1233 TAC TTG ATG TC-3' (ADAM10 #1) and 5'-GGA CTT CTT CAC TGG ACA CG-3'  
1234 (ADAM10 #2) and 5'-CTT AAG GTG AGC CTG ACT CT-3' (ADAM10 #3) for the  
1235 establishment of ADAM17-knockout cells. Pooled HEC50B cells infected with  
1236 pseudotype viruses were selected with 1 µg/mL puromycin for 1 week.

1237

1238 **S9 Fig. Effects of drugs on SARS-CoV-2 infection.**

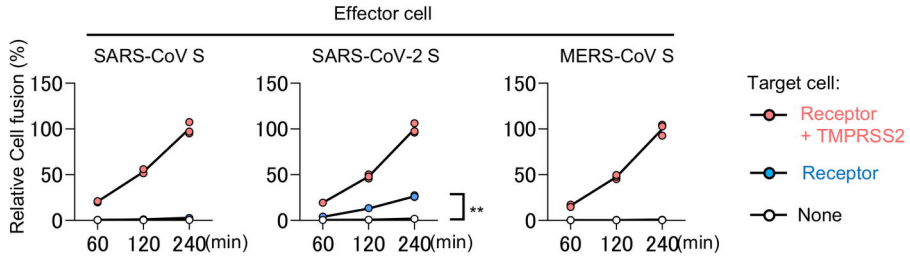
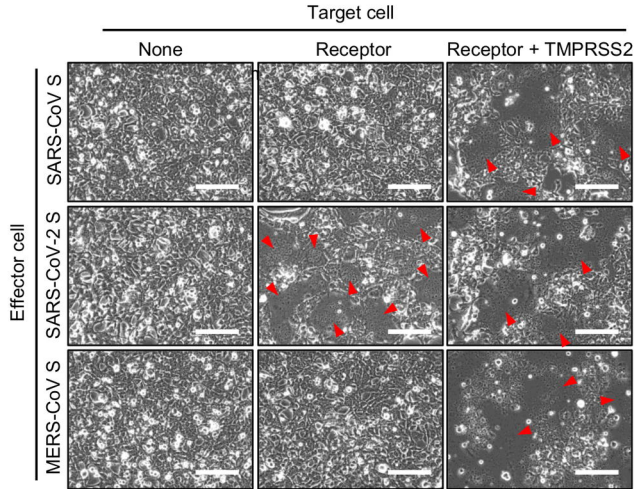
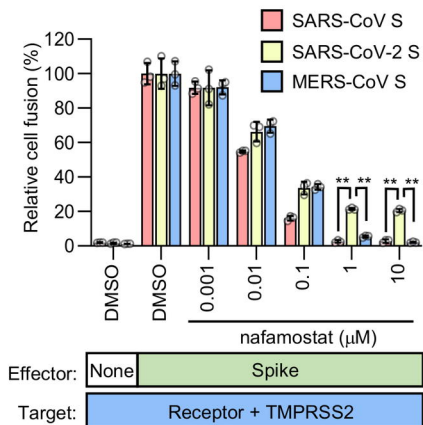
1239 (a) Effects of the nafamostat on the SARS-CoV-2 infection in Calu-3, HEC50B, A704,  
1240 and VeroE6 cells. Values are means ± SD ( $n = 3$ /group). \*\*  $p < 0.01$ . (b) Effects of the  
1241 E-64d on the SARS-CoV-2 infection in HEC50B, A704, and VeroE6 cells. Values are  
1242 means ± SD ( $n = 3$ /group). \*  $p < 0.05$ , \*\*  $p < 0.01$ . (c) Effects of the NH<sub>4</sub>Cl on the SARS-  
1243 CoV-2 infection in HEC50B cells. Values are means ( $n = 2$ /group). The relative amount  
1244 of viral RNA in the cells was normalized to cellular *Rpl13a* mRNA expression in (a-c).

1245

1246 **S10 Fig. The metalloproteinase-dependent entry pathway of authentic SARS-CoV-**  
1247 **2 is involved in syncytia formation.**

1248 Phase contrast images of syncytia formation 24 h after SARS-CoV-2 infection in the  
1249 presence of inhibitors. Red arrowheads indicate syncytia formation Scale bars, 100 µm.

1250

**a****b****c****d**